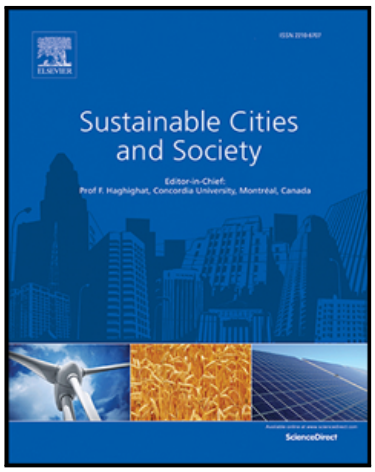

Seasonal variations of the dominant factors for spatial heterogeneity and time inconsistency of land surface temperature in an urban agglomeration of central China

Yang Xiang , Chunbo Huang , Xin Huang , Zhixiang Zhou , Xiaoshuang Wang

PII: S2210-6707(21)00561-8
DOI: https://doi.org/10.1016/j.scs.2021.103285
Reference: SCS 103285

To appear in: *Sustainable Cities and Society*

Received date: 9 March 2021
Revised date: 18 August 2021
Accepted date: 18 August 2021

Please cite this article as: Yang Xiang , Chunbo Huang , Xin Huang , Zhixiang Zhou , Xiaoshuang Wang , Seasonal variations of the dominant factors for spatial heterogeneity and time inconsistency of land surface temperature in an urban agglomeration of central China, *Sustainable Cities and Society* (2021), doi: https://doi.org/10.1016/j.scs.2021.103285

Seasonal variations of the dominant factors for spatial heterogeneity and time inconsistency of land surface temperature in an urban agglomeration of central China

Yang Xiang[a], Chunbo Huang[b], Xin Huang[a], Zhixiang Zhou[a,*], Xiaoshuang Wang[a]

[a] College of Horticulture and Forestry Sciences / Hubei Engineering Technology Research Center for Forestry Information, Huazhong Agricultural University, Wuhan, 430070 , PR China

[b] Research Center for Spatial Planning and Human-Environment System Simulation, School of Geography and Information Engineering, China University of Geosciences, Wuhan, 430078, PR China

author e-mail:

Yang Xiang: xy1091573805@hotmail.com

Chunbo Huang: huangchunbo@cug.edu.cn

Xin Huang: hxhanson@163.com

Zhixiang Zhou: whzhouzx@mail.hzau.edu.cn

Xiaoshuang Wang: lsourve@foxmail.com

***Corresponding author:**

Zhixiang Zhou Prof.

E-mail address: whzhouzx@mail.hzau.edu.cn, whzhouzx@126.com

Tel.: +86-02787284232

Permanent address: College of Horticulture and Forestry Sciences, Huazhong Agricultural University, Hongshan district, Wuhan 430070, PR China

Acknowledgments

This research was supported by the National Natural Foundation of China (31870701) and the Science and Technology Projects of Wuhan Municipal Bureau of Landscape and Forestry, Hubei, China (WHGF2018A11).

Declaration of Competing Interest

The authors report no declarations of interest.

1

Highlights

- Independence and interaction effect of influencing factors of land surface temperature (LST) were measured and quantified based on geo-detector.
- The driving mechanism of time inconsistency between different seasons as well as day and night of regional heat island (RHI) was explored based on a variety of statistical analysis methods.
- There were seasonal variations in the influencing factors on LST and time inconsistency of RHI.

Abstract: The urban heat island (UHI) effect is causing a series of environmental, energy and health problems. Studies on UHI are on the rise; however, some limitations still exist, such as the poor interaction of factors affecting land surface temperature (LST) and restriction of linear hypotheses from research method. To overcome these problems, we used geo-detector to measure the independent and interactive impacts on spatial heterogeneity of LST, and performed Spearman correlation, ordinary least-squares regression, all-subsets regression, and hierarchical partitioning analysis to explore the driving mechanism of time inconsistency of regional heat island (RHI). The results showed the most significant layers affecting

[1] Abbreviations: LST: land surface temperature; RHI: regional heat island; UHI: urban heat island.

spatial heterogeneity of LST in different seasons were landscape composition and biophysical parameters during daytime of relatively hotter seasons, climate conditions during winter daytime, climate conditions and biophysical parameters during nighttime, respectively. The wetlands proportion and albedo significantly influenced the time inconsistency of RHI between day and night. The dominant factors of time inconsistency of RHI between seasons were ΔNDVI, Δalbedo, Δalbedo, and Δsunshine duration during daytime, and Δsunshine duration, farmland proportion, Δair temperature, and forest land proportion during nighttime, respectively. These findings contribute to make scientific UHI adaptation strategies and promote sustainable development of cities and society.

Keywords: regional heat island; spatial heterogeneity; time inconsistency; seasonal variation

1. Introduction

In 2018, more than 55% of the world's population lived in cities, and this proportion is expected to increase to 68% by 2050 (UN, 2018). The rapid and drastic urbanization process, especially in developing countries, has greatly accelerated the transformation of natural landscape into more impervious surface within the urban areas, which, in turn, alters the radiative, thermal, moisture, roughness, and emission properties (Mathew et al., 2016). Surface modifications from urbanization have resulted in urban heat island (UHI) (Estoque et al., 2017). The urban heat island (UHI) effect, defined as the phenomenon that temperature in urban areas is higher than that in rural areas (Oke, 1973), has resulted in the intensification of extreme weather events (Patz et al., 2005; Zhong et al., 2017), an increase in energy consumption (Hirano et al., 2012; Santamouris et al., 2013; Yadav et al., 2017), the deterioration of air quality (Stathopoulou et al., 2008; Diem et al., 2017), adverse effects on health, and a rise in heat-related deaths (Tan et al., 2010; Heaviside et al., 2016; Arifwidodo et al., 2020). Conversely, UHI may have some benefits, including less energy

consumption for heating (Sun et al., 2014), improving the outdoor comfort, and reducing the road weather hazards (Stewart and Oke, 2012) and cold-weather related deaths (Macintyre et al., 2021) in cold climate. Understanding the mechanisms influencing land surface temperature (LST) plays an important role in the development of UHI adaptation strategies and helps to create eco-friendly and environmentally sustainable urban areas.

UHI research can be divided into three categories: the urban canopy layer (UCL), urban boundary layer (UBL), and surface urban heat island (SUHI) (Voogt and Oke, 2003). The UCL is an atmospheric heat island extending upwards from the surface to about mean building height (Voogt and Oke, 2003). The UCL heat island mainly relies on data from surface meteorological stations, field measurements, and model simulations to evaluate temporal and spatial changes (Ali et al., 2016; Li et al., 2019), influencing factors (Kotharkar et al., 2019), and impact on SUHI (Greene et al., 2018). However, the poor density induced by the small number of meteorological monitoring stations has limited the development of research on UCL. UBL heat island is also one of atmospheric heat islands and locates above the UCL (Oke., 1976). The UBL heat island is observed by special platforms, such as radiosondes, aircrafts, weather stations, and flux towers (Voogt and Oke, 2003). Studies on UBL heat island primarily rely on modeling (Oke, 1982), such as the Weather Research and Forecasting (WRF) model (Wang et al., 2019) and National Center for Atmospheric Research (NCAR) Mesoscale Model (Tong et al., 2005). SUHI is represented by thermal radiance received from the remote sensor (Voogt and Oke, 2003). Remote sensing images are used to determine LST to quantify the temporal and spatial characteristics (Liu et al., 2020), influencing factors (Li et al., 2011; Zhou et al., 2014; Peng et al., 2018), and mitigation strategies (Deilami et al., 2018). The easy access, wide spatial distribution, and significantly high temporal resolution of remote sensing promoted the development of research on SUHI (Peng et al., 2018).

The previously reported influencing factors of LST fall under four categories, namely, landscape metrics (Li et al., 2011; Chen et al., 2014; Estoque et al., 2017; Li

et al., 2017; Yang et al., 2017), socio-economic indicators [population, gross domestic product (GDP), and nighttime lights] (Zhou et al., 2014; Cui et al., 2016; Hu et al., 2019; Li et al., 2020a), climate conditions (Zhou et al., 2014; Du et al., 2016; Rui et al., 2018; Li et al., 2020b), and biophysical parameters (normalized difference vegetation index, albedo, and digital elevation model) (Li et al., 2011; Chen et al., 2012; Zhou et al., 2014; Guo et al., 2015; Li et al., 2020b).

It is known that LST is influenced by several factors. Numerous statistical methods were used to explore the relationship between LST and the influencing factors, among which ordinary least-squares (OLS) regression is a common method (Deilami et al., 2018; Peng et al., 2018). However, there are still several limitations in the previously used methods. First, most of the methods used to investigate LST and its influencing factors were based on linear assumptions. It is difficult to detect the influence mechanism of LST based on linear assumptions because of the complexity of the spatial distribution of LST (Hu et al., 2020). Second, the spatial heterogeneity of LST is the outcome of the conjoint effect of various factors instead of being caused by a particular influencing factor (Peng et al., 2018). Previous studies have failed to solve interactions and collinearity problems among different influencing factors (Peng et al., 2012; Zhou et al., 2014; Zhou et al., 2019; Zhou et al., 2020), thus substantially hindering insight into the influence mechanism of LST, affecting the accuracy of research results and the formulation of UHI mitigation strategies. Third, most previous studies have focused on single or several large cities, and LST of urban agglomerations is poorly understood (Zhou et al., 2018). Finally, prior studies have not been able to incorporate the effects of these types of influencing factors on UHI (Peng et al., 2018), and explore the driving mechanism of time inconsistency between the UHI in different seasons as well as day and night.

In this study, RHI is defined as the relatively high LST classification in urban agglomeration (Yu et al., 2019). Moreover, time inconsistency of RHI refers to the dissimilarity between different seasons as well as night and day—ΔRHI—which is the difference between two-time nodes in the same spatial unit. The main purpose of this

study is (1) to compare the spatial characteristics of high temperature regions in different day and night of seasons based on standard deviation ellipse (2) to explore the spatial heterogeneity of LST and interaction of factors influencing LST based on the geo-detector (3) to quantify the relationship between the time inconsistency of RHI and potential driving factors based on Spearman correlation, ordinary least-squares regression, all-subsets regression, and hierarchical partitioning analysis. Therefore, this study is expected to provide urban planners and policy makers with the basic understanding of the mechanisms that influence LST to develop sustainable urban planning and policies to mitigate the effects of UHI.

2. Materials and Methods

2.1 Study area

The urban agglomeration in the middle reaches of the Yangtze River (UAMRYR) is located in the Hubei, Hunan, and Jiangxi provinces in central China (110°15-118°29E, 25°59-32°64N), and is a crucial part of the Yangtze River Economic Belt in China, including 31 cities (Fig. 1a). As a national urban agglomeration formed by Wuhan city circle, urban agglomeration around Changzhutan and Poyang Lake urban agglomeration, the UAMRYR covers an area of approximately 326,100 km^2, and the GDP reached 805.7 billion RMB Yuan (Chinese currency) in 2018, with a population exceeding 125 million in 2018 (Dai et al., 2020). The UAMRYR has a subtropical monsoon climate with abundant rainfall and sunshine. Terrain is generally low in the middle and high all around, and water resources are abundant (Chen et al., 2019), including the Yangtze River, Dongting Lake, and Poyang Lake. Fig. 1b showed land cover of the study area in 2010.

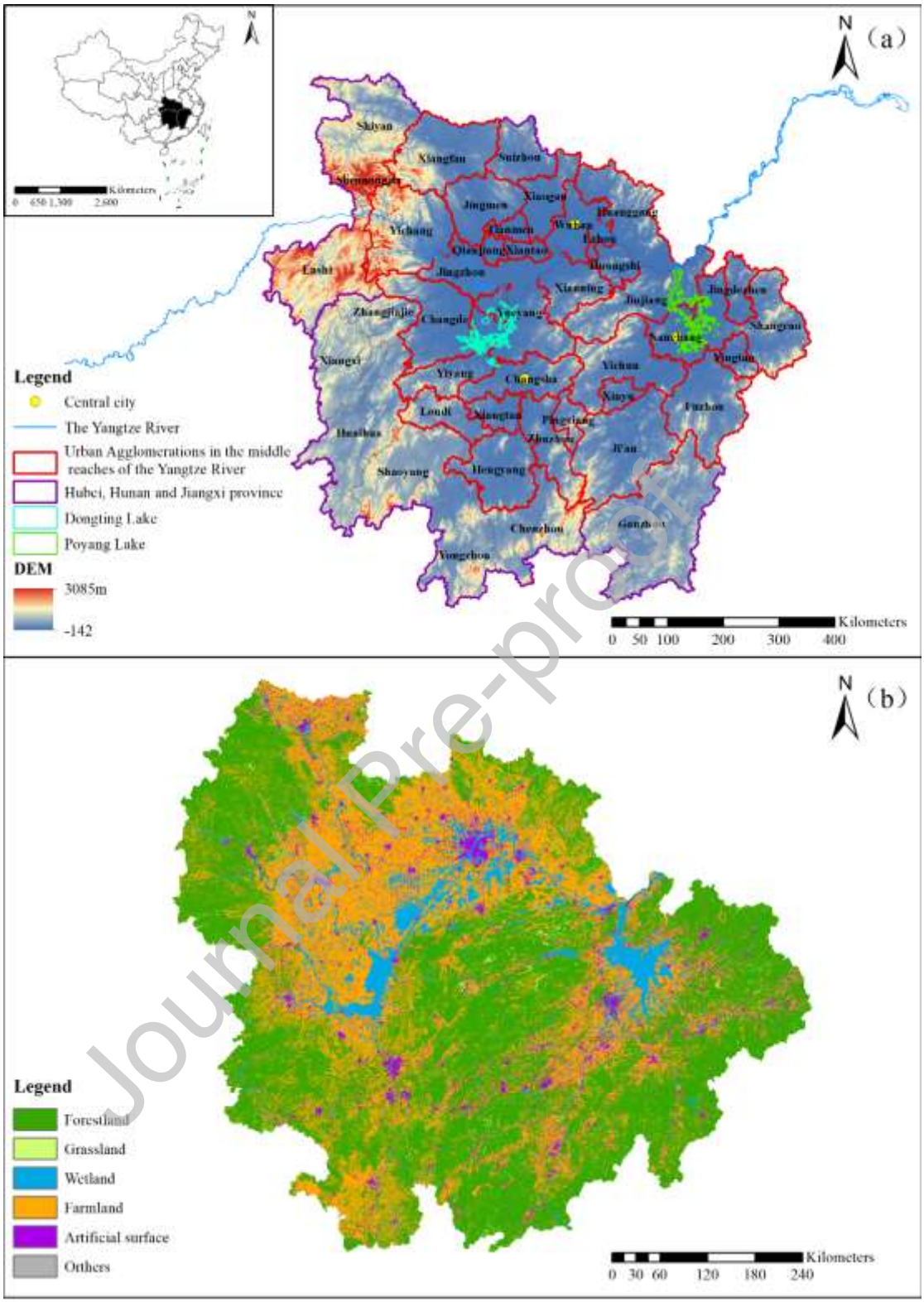

Fig. 1 Location and land cover of the study area.

Note: a is location map of the study area, and b is the land cover map of the study area.

2.2 Multi-source data

The following data were used to examine the interrelation between impact factors and LST in this study:

1. The LST was derived from the China 1-km LST monthly synthetic product (MYDLT1M, Terra) in 2010. The dataset covers all the land boundaries of China and was synthesized from a reliable and cloudless MOD11A1 dataset using the average value method. The missing value in the dataset was filled by the average value of the data in the nearby one to two years. The data was extracted from the geospatial data cloud of the Computer Network Information Center of The Chinese Academy of Sciences (http://www.gscloud.cn/).

2. Land use and land cover (LULC) products were come from "China Cover 2010" dataset, which was interpreted using the object-oriented method at a spatial resolution of 30 m in 2010. The dataset was divided into six categories: (1) forest land (including broad-leaved forest, coniferous forest, mixed forest, shrub forest, garden), (2) grassland, (3) wetlands (including forest wetlands, shrub wetlands, herb wetlands, lake, river), (4) farmland (including paddy field and dry land), (5) artificial surface (residential land, industrial land, traffic land, quarry), and (6) other land (sparse woodland, sparse shrub, sparse grass, bare land, sand land, saline land, glacier, moss). The overall accuracy of the dataset was 91% (Wu et al., 2014; Lei et al., 2014; Zhang et al., 2014). The LULC types of forest land, grassland, wetlands, farmland and artificial land were selected for this study. The dataset was obtained from the National Science and Technology infrastructure platform, National Earth System Science Data Center (http://www.geodata.cn).

3. Climate conditions data were obtained from the monthly dataset of surface climate data in China. We selected meteorological stations from Hubei, Hunan, Jiangxi, and the nine surrounding provinces and used the cokriging method to interpolate the monthly meteorological data. Then, the seasonal data were calculated based on the monthly meteorological data. The dataset was derived from the China

Meteorological Data Network (http://data.cma.cn/). The spatial distribution of meteorological stations in study areas is shown in Fig A.1.

4. Population data were obtained from the Gridded Population of the World Version 4 (GPWv4) dataset (https://sedac.ciesin.columbia.edu/) in 2010 at 30 arc-seconds output resolution.

5. GDP data were derived from the grid data set of China's GDP spatial distribution kilometers in 2010 at 1 km spatial resolution, supported by the Resource and Environment Science and Data Center (http://www.resdc.cn/). The value of each grid in the GDP dataset was the sum of GDP per square kilometer.

6. Nighttime light was used to monitor and evaluate social economy and urbanization dynamics (Zhang et al.,2011; Hu et al., 2020), as it is often considered to be one of the social economic indexes that influence LST (Peng et al., 2018). Nighttime light data were obtained from DMSP-OLS nighttime light in 2010 at 30 arc-seconds spatial resolution, provided by National Centers for Environmental Information (http://www.ngdc.noaa.gov/).

7. Albedo reflects solar radiation and surface heat storage (Peng et al., 2012), and is significantly associated with LST (Yao et al., 2018). Albedo data were derived from albedo product in the GLASS dataset in 2010, which is synthesized based on the daily resolution of MOD09GA (Terra) and MYD09GA (Aqua) after filtering and filling at 1 km spatial resolution. The albedo product of GLASS dataset can capture the variation of surface albedo better than MODIS (Liu et al., 2013), provided by the National Science and technology infrastructure platform, National Earth System Science Data Center (http://www.geodata.cn).

8. DEM describes the topography and elevation of study area and has a significant correlation with LST (Li et al., 2017; Li et al., 2020b). DEM were obtained from SRTM-DEM data at 90 m spatial resolution, supported by the Resource and Environment Science and Data Center (http://www.resdc.cn/).

9. NDVI reflects the state of vegetation coverage and is significantly correlated with LST (Yadav et al., 2014; Peng et al., 2018). NDVI were extracted from the

MODIS NDVI product (MYD11A3) in 2010, and the product was synthesized monthly by the U.S. Geological Survey at 1 km spatial resolution (https://e4ftl01.cr.usgs.gov/).

2.3 Determination of influencing factors

Five layers, including landscape composition, landscape configuration, biophysical parameters, social economy, and climate conditions were selected as influencing factors (Table 1). A large number of studies showed that landscape composition and landscape configuration had significant impact on LST. Therefore, based on previous research (Zhou et al., 2011; Zhang et al., 2015; Peng et al., 2018), five landscape composition and four landscape configuration indexes were commonly used in this study. The five landscape composition indicators are percentages of forest land, grassland, wetlands, farmland, and artificial surface, respectively. The four landscape configuration metrics included the largest patch index (LPI), mean shape index distribution (SHAPE_MN), patch density (PD), and Shannon's diversity index (SHDI). The NDVI (Peng et al., 2018), albedo (Peng et al., 2012; Zhou et al., 2014), and DEM (Chen et al., 2012) in the surface biophysical parameters are often considered as influencing factors of LST. Socio-economic indicators included population (POP), GDP, and nighttime light (NL). Climate conditions factors also substantially explain the spatial heterogeneity of the UHI (Yao et al., 2018; Manoli et al., 2019). Therefore, seasonally mean air temperature, seasonally mean air relative humidity, seasonally mean rainfall, seasonally mean sunshine duration, and seasonally mean wind speed were considered as climate conditions factors in this study. Table A.1 lists the selected literature sources on the influencing factors of LST.

Table 1. Influencing factors of LST used in this study.

Categories of variables	Variables	Meaning of variables
Landscape	PD	Density of the landscape patches in grid

configuration	LPI	Largest patch index of the landscape in grid
	SHDI	Shannon diversity index of landscape in grid
	SHAPE	Mean shape index distribution of the landscape in grid
Landscape composition	FL	Percentage of forest land in grid
	GL	Percentage of grassland in grid
	WL	Percentage of wetlands in grid
	F	Percentage of farmland in grid
	AL	Percentage of artificial surface in grid
Social economy	POP	Mean value of POP in grid
	GDP	Mean value of GDP in grid
	NL	Mean value of nighttime light in grid
Climate conditions	Air	Mean value of air temperature in grid
	Hum	Mean value of air relative humidity in grid
	Rain	Mean value of rainfall in grid
	Sun	Mean value of sunshine duration in grid
	Wind	Mean value of wind speed in grid
Biophysical parameters	Albedo	Mean value of albedo in grid
	NDVI	Mean value of NDVI in grid
	DEM	Mean value of DEM in grid

2.4 Delineation of seasons

The UAMRYR is located in a subtropical monsoon zone. We selected temperature and precipitation levels from meteorological stations positioned at a median elevation in different climate regionalization to divide the seasons. First, the monthly datasets from surface cumulative annuals in China (1981–2010) were collected. Following this, the meteorological stations in the study area were divided into two categories, namely, the north and middle subtropical zone, based on the

classification of climate regionalization (Fig A.2) by the National Meteorological Administration of China (supported by the Resource and Environment Science and Data Center (http://www.resdc.cn/). The meteorological stations positioned at a median elevation were used to describe different the regional climate characteristics. Fig. 2 showed that the temperature and precipitation at the meteorological stations in different climatic regions were similar, with the temperature peaking in July, and then gradually decreasing, with the precipitation peaking in June, and then gradually decreasing. January, February, and December had the lowest temperatures and were, therefore, referred to as winter. March, April, and May were determined to be spring, and September, October, and November referred to as autumn. June, July, and August were the hottest months of the years and were, thus, determined to be summer.

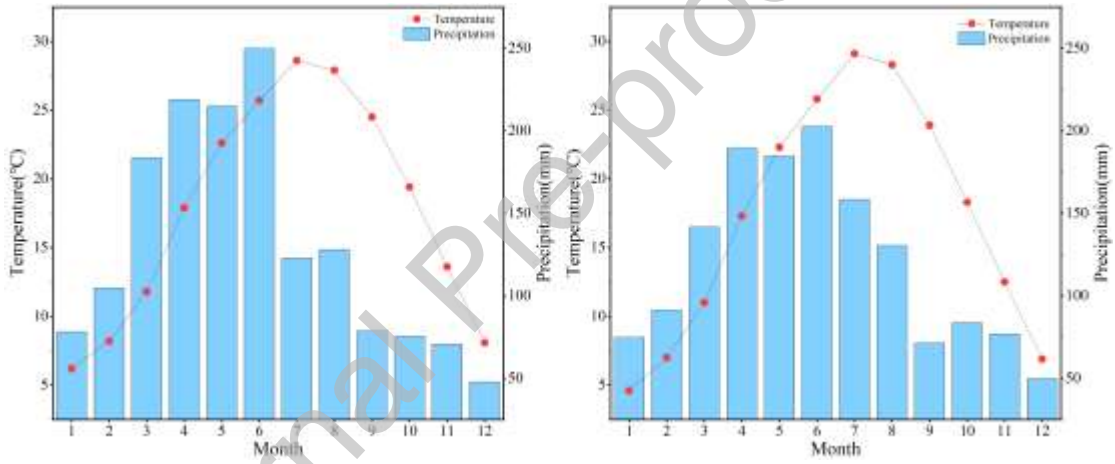

Fig. 2 Temperature and precipitation of the cumulative annuals monthly mean:
a) the middle subtropical zone, b) the north subtropical zone.

2.5 Direction and distribution of LST

The standard deviation ellipse (SDE), as a directional distribution analysis method, depicts the spatial characteristics of geographic elements (central trend, dispersion, and directional trend) based on the average center of discrete points and the standard distance of other points away from the average center. The SDE is calculated as follows:

$$SDE_x = \sqrt{\frac{\sum_{i=1}^{n}(x_i-\overline{X})^2}{n}} \text{ and } SDE_y = \sqrt{\frac{\sum_{i=1}^{n}(y_i-\overline{Y})^2}{n}},$$

where x_i and y_i are the coordinates of grid$_i$, $\overline{X}$ and $\overline{Y}$ represent the average central coordinate of UAMRYR, and n is the total number of grids.

The SDE has been used in the past to analyze the temporal and spatial characteristics of annual PM2.5 concentration (Peng et al., 2016; Shi et al., 2018b), vegetation cover (Yuan et al., 2020), and other geographical elements.

The standard deviation classification method with an interval of 1.0 was used to divide the LST intensity into five classifications (Firozjaei et al.,2018; Yang et al., 2019; Firozjaei et al., 2020), namely, low, sub-low, medium, sub-high, and high (Table A.2). RHI was characterized by five classifications of LST. The SDE method was used to quantify the spatial characteristics of sub-high and high categories in different seasons.

2.6 Geo-detector model

Geo-detector, a statistical analysis method for detecting spatially stratified heterogeneity, can be used to overcome the problem of the linear hypotheses and collinearity (Wang et al., 2017), and it can detect the explanatory power of geographical phenomena between two factors. Geo-detector has been widely used in the driving force analysis of population distribution (Wang et al., 2018c), health risk assessment (Wang et al., 2010), air pollution (Bai et al., 2019), groundwater pollution (Zhu et al., 2019), heavy metal risk (Shi et al., 2018a; Wang et al., 2018b), ecosystem services (Chen et al., 2020), and urban forests (Duan et al., 2020). Factor and interaction detectors were used to analyze the association between LST and the influencing factors based on a 3000 × 3000m grid.

2.6.1 Factor detection

Factor detection was mainly used to detect the extent to which the influencing factor explains the spatial heterogeneity of LST. It is measured by the q value via the

following formula:

$$q = 1 - \frac{\sum_{h=1}^{L} N_h \sigma_h^2}{N\sigma^2} = 1 - \frac{SSW}{SST}$$

$$SSW = \sum_{h=1}^{L} N_h \sigma_h^2, SST = N\sigma^2$$

where, L is the stratification of variable LST or factor X, that is, classification; N_h and N are the number of layers, h and the entire area, respectively; σ_h^2 and σ^2, are the variances of layer h and the entire area Y, respectively; SSW and SST are the sum of intra-layer variance and the total variance of the entire area, respectively; and the range of q is [0,1]. The larger the value of q, the greater the interpretation of LST by the impact factor X, and the value of q indicates that the impact factor X explains 100*q% of the spatial heterogeneity of LST.

2.6.2 Interaction detector

Interaction detection was used to quantify the explanatory power of X_1 and X_2 on the spatial heterogeneity of LST. Similar to factor detection, interactive detection is measured by the q value and $q \in [0,1]$. The larger the q value, the greater the explanatory capacity on the spatial heterogeneity of LST.

2.7 Data discretization

The geo-detector model is mainly concerned with models of spatial heterogeneity, and the independent variables of the model need to be discretized into type variables. However, it is difficult to select the number of categories: excessive classifications are superfluous, whereas few classifications cannot reflect the abundance and diversity of variables. Based on the related study by Cao et al. (2015), a discretization scheme with the largest q value was conducted. Several common discretization methods were used for discrete independent variables, such as natural breakpoint, geometric interval, equal interval, and quantile. Several indicators (NDVI, NL, FL, WL, AL, POP, GDP, and Sun) were used to judge the q value of each method in July (Fig A.3). Finally, the

quantile method was used in this study and divided into 10 grades.

2.8 Potential driving forces of time inconsistency of RHI

Time inconsistency refers to the dissimilarity of RHI from the same spatial units in different seasons as well as day and night. A variety of statistical analysis methods was used to identify the relationship between ΔRHI and potential driving forces. First, a Spearman correlation analysis was performed to quantify the correlation between 17 influencing factors (Table 1) and ΔRHI. Second, candidate factors that passed the significance test in the OLS coefficients at the 0.05 level were identified. All-subset regression was conducted to select the significant driving factors in the model with the highest adjusted R^2. Finally, based on the "hier.part" package of R, hierarchical partitioning (HP) was conducted to identify the independent effects of the significant driving factors on ΔRHI. Compared with the traditional regression analysis methods, the HP analysis is not affected by multicollinearity; therefore, it is favorable for multi-dimensional environmental data analysis (Peng et al., 2018).

3. Results

3.1 Spatiotemporal pattern of LST in different seasons

LST in different seasons exhibited similar patterns (Fig. 3). During daytime, the LST generally exhibited a low north and high south distribution patterns. The low-temperature areas were mainly distributed in the northwest of the UAMRYR, near the high-altitude areas of Shennongjia and Enshi and around the Yangtze River. Meanwhile, the high-temperature areas were mainly concentrated over the urban agglomeration in the south. The temperature in the northwestern part of the urban agglomeration was lower at night, which was similar to that during daytime. However, the area near the Yangtze River did not show obvious low-temperature areas compared with that during daytime, which may be attributable to the larger specific

heat capacity of water. The box plots in Fig. 4 depict the distribution characteristics of LST in day and night at seasonal level.

The spatial and temporal patterns in the high-temperature region of the LST were evaluated using SDE. The results of SDE showed that the average centers of day and night in different seasons were located in the central and southern parts of the study areas (Fig. 5), but the average centers and direction distribution parameters of seasons still varied (Table 2). During daytime of different seasons, the center of high temperature areas (average center) gradually moved from the east of Changsha in spring to the southeast of Yueyang (offset by 68.53km) in summer, and then moved to the south by 31.34 km in autumn, and finally moved to the northwest of Yichun City in winter (offset by 102.40km). The annual average center during the day was in the east of Changsha. During nighttime of different seasons, the center of the high temperature areas shifted from the southeast of Yueyang in spring to the north in summer by 67.40 km, then shifted to the northwest of Yichun City along the southeast direction in autumn (offset by 73.27 km), and finally shifted to the south by 105.83 km in winter. The annual average center during the nighttime was east of Changsha.

The spatial distribution trend of the high-temperature areas was determined using the major and minor axes of the SDE. The SDE results showed that the parameters of SDE in the high-temperature region change constantly in the day and night of different seasons, which indicated the irregularity in the seasonal variation of the high-temperature region. From the daytime of spring to the daytime of summer, the major axis and minor axis of the ellipse increased, and the ellipse tended to expand, suggesting that the high-temperature areas in the outer edge of the ellipse grew faster than that at the center of the ellipse. From the daytime of summer to the daytime of autumn, the shortening of the major and minor axes of the ellipse and the shrinking of the ellipse indicated that the growth rate of high-temperature areas at the center of the ellipse increased faster than that outside the ellipse. From the daytime of autumn to the daytime of winter, the shortening of the major axis and lengthening of the minor axis illustrated that the growth rate in the east–west direction was faster than that in

the north–south direction. From the nighttime of spring to that of summer, the nighttime of summer to that of autumn, and the nighttime of autumn to that of winter, the shortening of the minor axis and the lengthening of the major axis indicated the growth rate of high-temperature areas from the north–south direction and was significantly higher than that from the east–west direction.

The changing trend of the spatial direction of the high-temperature areas was reflected by the azimuth of the major axis of the ellipse. During the day of spring, summer, autumn, and winter, the azimuth of the major axis of the ellipse first increased from spring to summer, reached its peak in summer, and then gradually decreased in autumn and winter. This indicated that from spring to summer, the southeast of the UAMRYR was more influential in the high temperature areas, while in autumn and winter, the northeast of the UAMRYR had greater influence on the high-temperature area. During the nighttime of spring, summer, autumn, and winter, the azimuth increased from spring to summer, and then decreased to the lowest point in autumn, and finally increased in winter. This meant that from spring to summer, the influence of the southeast of the UAMRYR on the high-temperature area increased, and then the influence of the northeast on the high-temperature area gradually increased in autumn, and the influence of the southeast on the high-temperature area increased in winter.

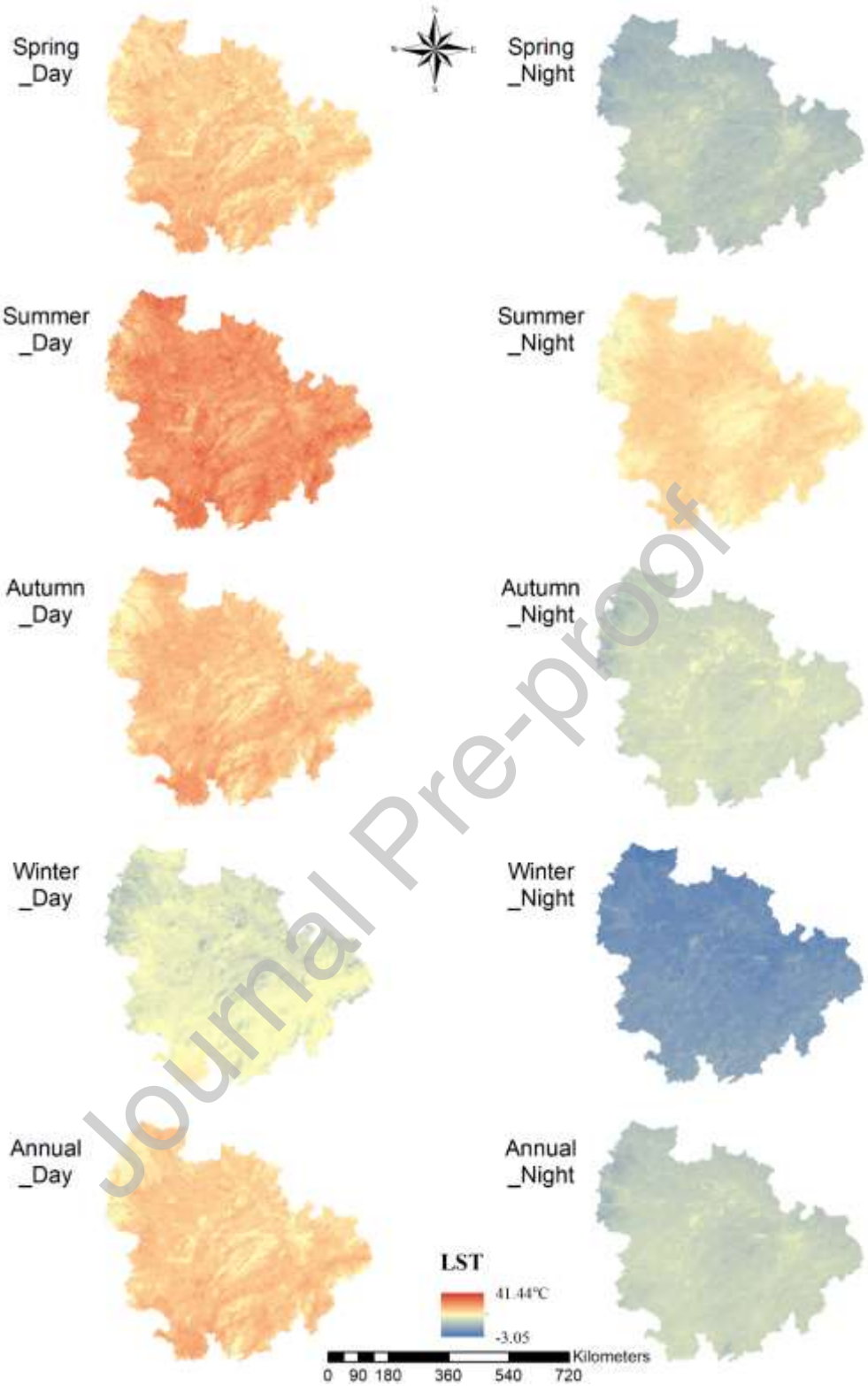

Fig. 3 Seasonal spatial variability of LST in the UAMRYR.

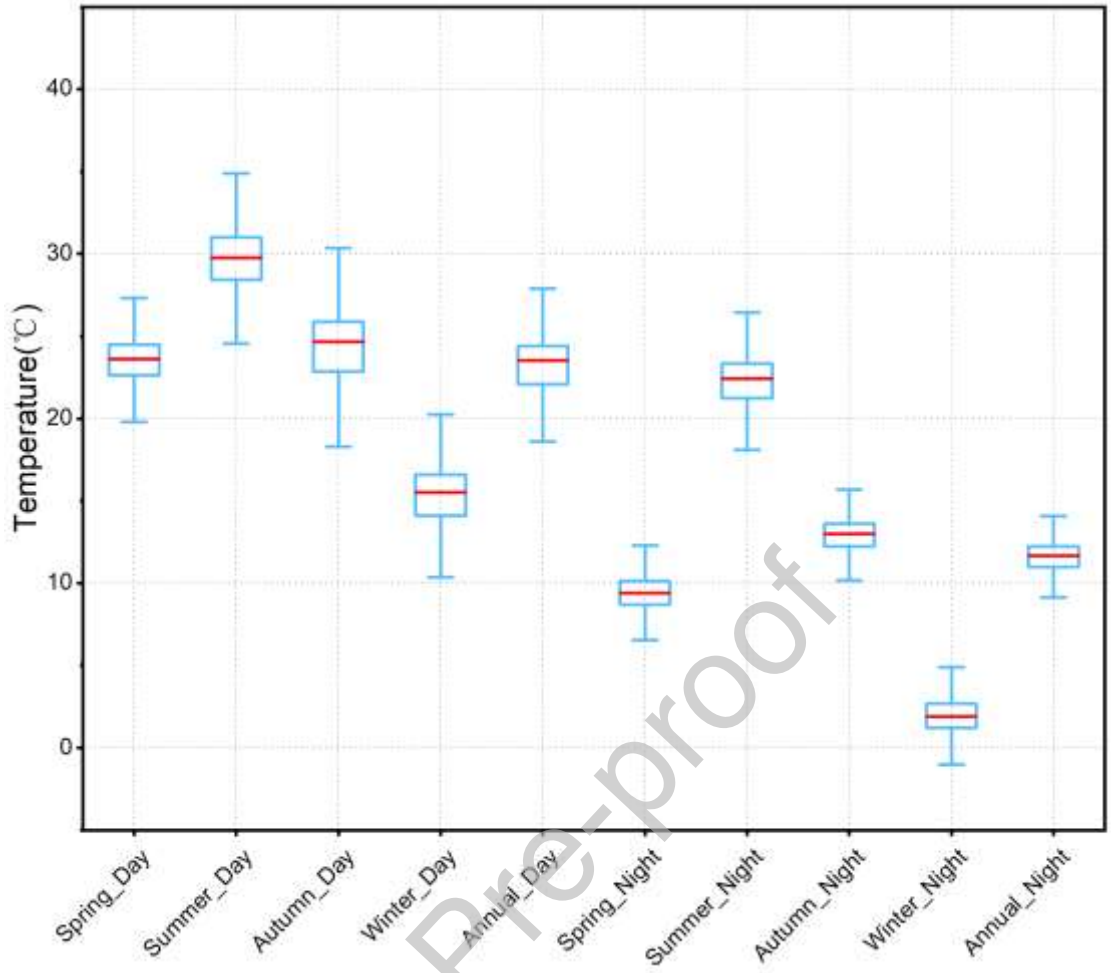

Fig. 4 Box plots of the LST in the day and night at seasonal level.

Note: The red lines represent the median values, whereas the blue whiskers are interquartile range of 1.5 times.

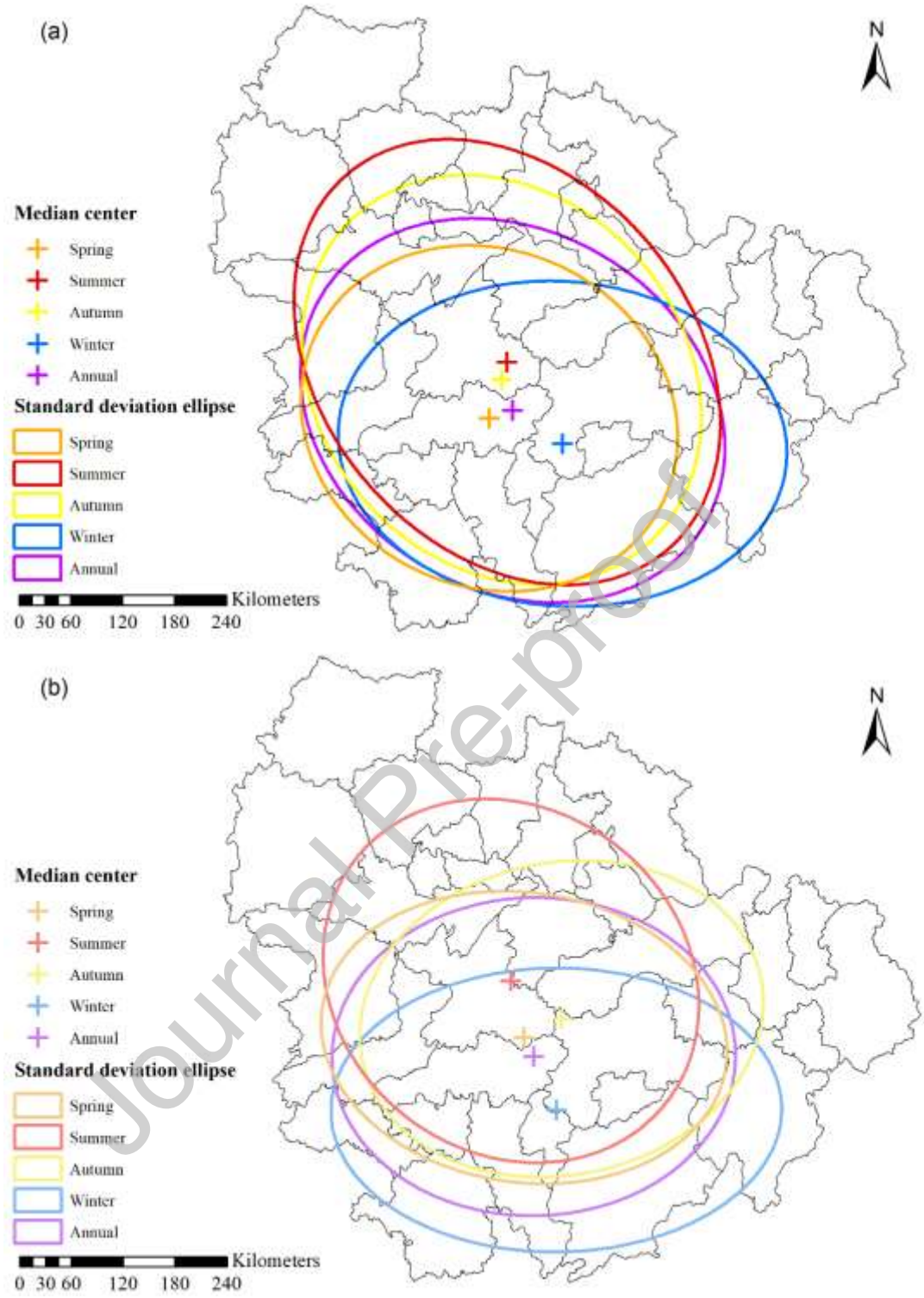

Fig. 5 Result of the standard deviation ellipse of high-temperature areas (high, sub-high) in the day and night of different seasons.

Table 2 The parameters of SDE of high temperature areas (high, sub-high) in the day and night of different seasons.

Time	Short axis (X) (km)	Long axis (Y) (km)	Rotation
Spring_Day	223.24	194.81	115.70
Summer_Day	285.87	214.16	139.58
Autumn_Day	254.60	211.68	138.85
Winter_Day	260.32	188.03	94.75
Annual_Day	258.55	207.58	121.39
Spring_Night	236.37	167.81	98.25
Summer_Night	228.56	198.83	128.30
Autumn_Night	180.88	235.74	78.38
Winter_Night	164.45	261.11	89.58
Annual_Night	184.29	233.68	88.94

3.2. Dominant impact factors of LST in different seasons

The spatial heterogeneity of LST in different seasons was analyzed using the factor detector in geo-detector and the potential influencing factors in day and night of different seasons were used for comparison. The results showed significant differences in the potential impact factors in day and night of different seasons. Fig. 6 showed the calculation results of the q value for the day and night of each season. Most factors passed the significance test at a significance level of 0.01 except for GL. The q values of the landscape composition and biophysical parameters were relatively high during the daytime of the hot season (spring, summer and autumn) and annual, whereas the q values of the climate conditions layer were dominant during the daytime of the winter. The climate conditions layer during the nighttime of spring, autumn, winter, and annual showed a higher q value than other layers, whereas during the nighttime of the summer, biophysical parameters and landscape composition were the primary. More specifically, during the daytime of spring, summer, autumn, winter, and annual, the dominant factors that explained the spatial heterogeneity of LST

ranked as follows: DEM (0.29), DEM (0.43), DEM (0.57), Air (0.38), and DEM (0.48), whereas Rain (0.42), DEM (0.68), DEM (0.32), Air (0.55), and Air (0.41) were highest q value during the nighttime of spring, summer, autumn, winter and annual. Understanding the spatial heterogeneity of LST from different seasons is beneficial to urban planning.

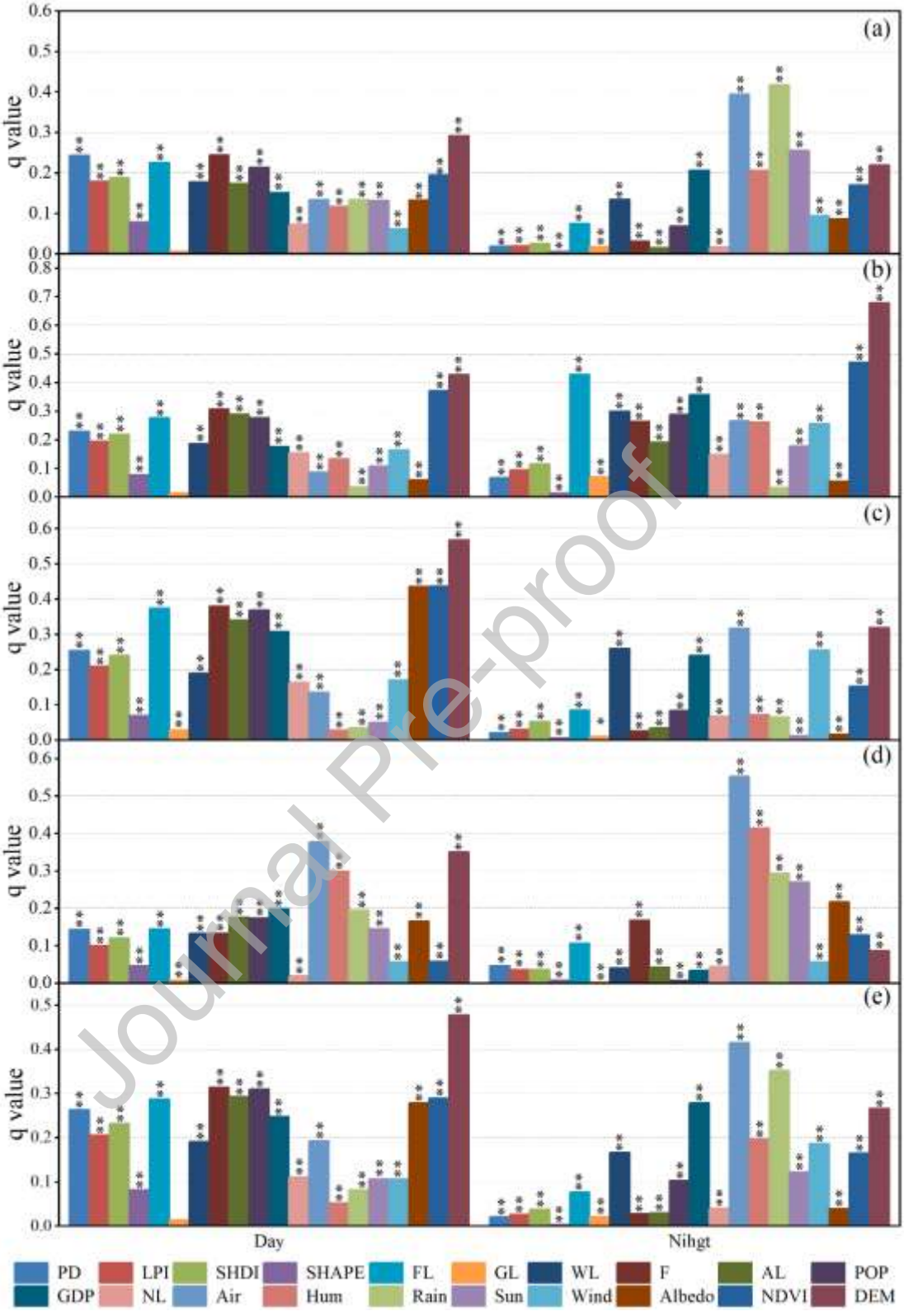

Fig. 6 q values of impact factors in different season.

Note: a, b, c, d, e represent spring, summer, autumn, winter and annual, respectively. *, and ** denote that q value is significant at levels of 0.05 ($p<0.05$), 0.01 ($p<0.01$),

respectively.

3.3 Interaction between the impact factors of LST in different seasons

The interaction between the two influencing factors in different seasons was compared using the interaction detector in the geo-detector model. The influencing factors of different layers were used to analyze their interaction. In addition, the interaction q value of the same influencing factor does not change compared with a single q value. Finally, twenty interaction factors were used to quantify the interaction between the influencing factors. The results of the interaction detector showed that the interaction varied greatly in different seasons (Fig. 7). Specifically, during daytime of spring, summer, autumn, winter and annual, the interaction q values with higher explanation capacity of the spatial heterogeneity of LST were as follows: F ∩ Sun (0.48) > DEM ∩ Rain (0.47) > DEM ∩ Sun (0.46), DEM ∩ NDVI (0.55) > WL ∩ NDVI (0.53) > DEM ∩ Rain (0.51), DEM ∩ Sun (0.70) > NDVI ∩ Air (0.66) > NDVI ∩ DEM (0.64), DEM ∩ Air (0.69) > albedo ∩ Air (0.66) > Air ∩ F (0.65), Air ∩ NDVI (0.64) > Sun ∩ DEM (0.64) > Air ∩ DEM (0.61). During nighttime of spring, summer, autumn, winter and annual, the dominant interaction factors and q values of LST were as follows: DEM ∩ Air (0.60) > Air ∩ Rain (0.59) > Rain ∩ Sun (0.58), Wind ∩ DEM (0.75) > DEM ∩ Sun (0.74)> DEM ∩ Rain (0.72), Air ∩ WL (0.55) > DEM ∩ Air (0.54) > NDVI ∩ Air (0.51), Sun ∩ Air (0.65) > F ∩ Air (0.63) > Rain ∩ Air(0.62), DEM ∩ Air (0.61) > NDVI ∩ Air (0.60) > Air ∩ WL (0.60).

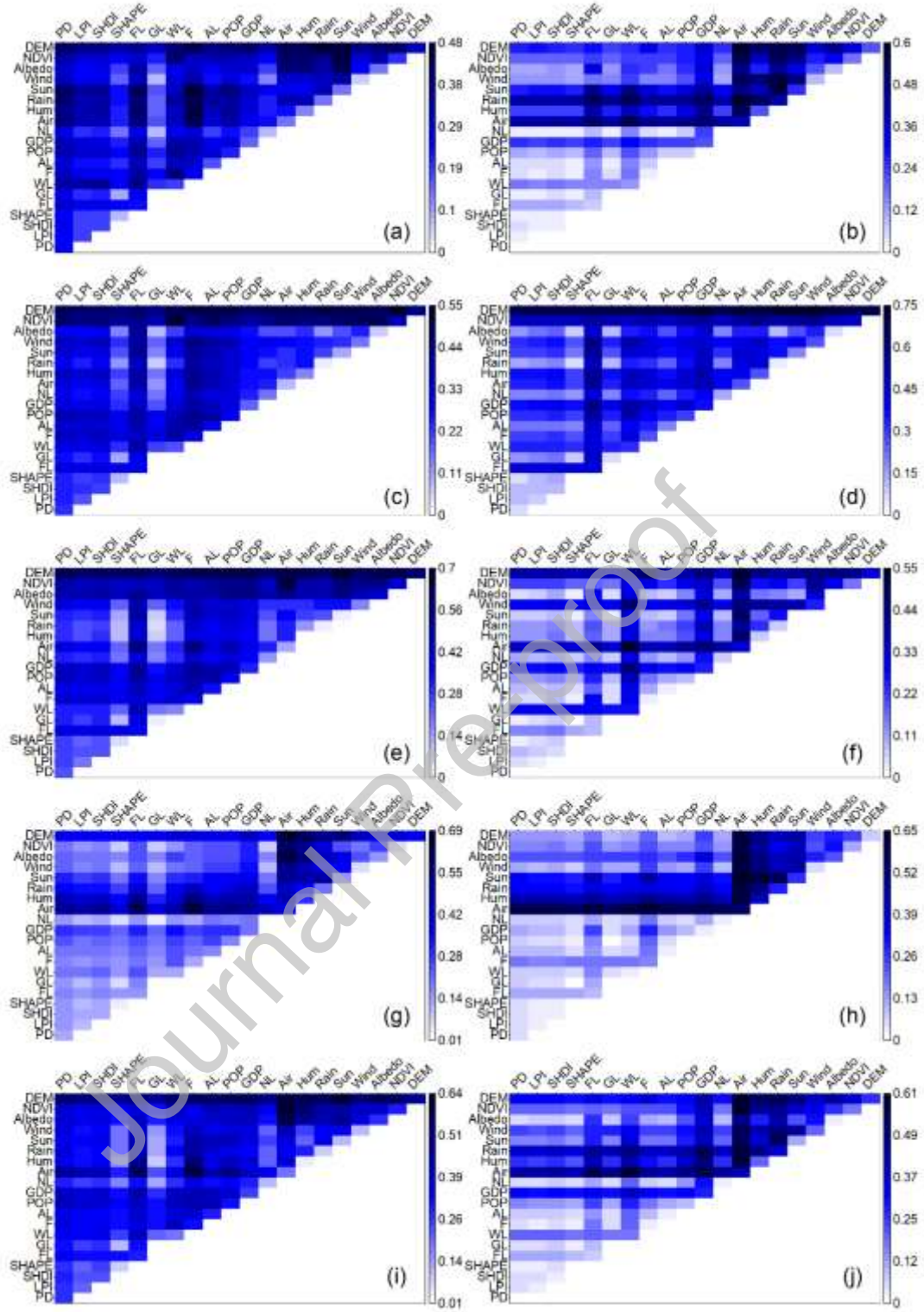

Fig. 7 Interaction between the factors influencing LST in different seasons.

Note: a-j represent spring day, spring night, summer day, summer night, autumn day, autumn night, winter day, winter night, annual day and annual night, respectively.

3.4 Analysis of potential drivers of ΔRHI

We selected 20 metrics (Table 1) as driving factors. The seasonal variables, namely, Air, Hum, Sun, Wind, albedo, and NDVI, were replaced with ΔAir, ΔHum, ΔSun, ΔWind, Δalbedo, and ΔNDVI, respectively. ΔRHI was regarded as the dependent variable. The heat map was used to show the strength of the correlations between the driving factors and ΔRHI. The correlations significantly changed with seasonality and day-night differences in terms of which driving factors and how strongly were they correlated with ΔRHI (Fig 8). Most driving factors were statistically significant ($p < 0.01$). In many cases, albedo (Δalbedo) showed a dominant and negative correlation with ΔRHI. Moreover, LPI, Air, and Rain were positively correlated with ΔRHI between day and night, whereas SHAPE, SHDI, PD, and AL were negatively correlated with ΔRHI. FL, DEM, and Δ Air showed a relatively higher and positive coefficient in the ΔRHI of autumn–winter, whereas NL was negatively correlated with ΔRHI. DEM, ΔWind, and ΔSun showed a relatively high and negative correlation with the ΔRHI of spring–summer, whereas ΔHum showed a high and positive correlation with ΔRHI.

The OLS regression was used to select significant driving factors of ΔRHI, and then the driving factors that passed the significance test ($P < 0.05$) were put into the all-subset regression. Then, the optimal model (Table A.3, Table A.4, Table A.5) was obtained based on the adjusted R^2 test of models. Finally, the independent contribution rate of different influencing factors to ΔRHI was quantified using HP analysis.

The results of HP analysis (Fig. 9a) showed that WL and albedo had a strong ability to explain ΔRHI between day and night. Specifically, WL (43.37%) and albedo (21.36%) were the dominant driving factors in spring; WL (63.59%) had the largest independent contribution rate to ΔRHI in summer. Albedo and WL were the most important factors, independently contributing 37.82% and 30.77%, respectively; albedo (33.05%), DEM (22.95%) made larger independent contributions to ΔRHI; WL (43.03%) and albedo (28.78%) had a higher annual contribution rate. The

independent contribution rate of WL to ΔRHI increased first and then decreased with the change in temperature during the four seasons. In the season of higher temperature, the effect of WL on ΔRHI was dominant, but the influence of WL on ΔRHI declined as temperature decreased, which complicated the driving mechanism of ΔRHI. Albedo initially exhibited an increasing trend and then decreased in spring, autumn, and winter.

The results of the HP analysis indicated significant differences among the dominant driving factors of ΔRHI during the day of all seasons (Fig. 9b). ΔNDVI, ΔWind, and ΔSun were the dominant factors with higher contribution rates to ΔRHI between the day of spring and summer, independently contributing 21.20%, 19.53%, and 19.49%, respectively; Δalbedo (26.89%), ΔSun (23.68%), and ΔHum (16.37%) showed strong ability to explain ΔRHI between the day of summer and autumn; Δalbedo (23.86%), NL (16.94%), ΔRain (15.92%) made larger independent contributions to ΔRHI between the day of autumn and winter; ΔSun (52.08%), NL(12.10%), ΔAir (11.51%) had a higher contribution rate to ΔRHI between the day of winter and spring.

The results of the HP analysis showed significant differences among the dominant factor of ΔRHI during nighttime in all seasons (Fig. 9c). ΔSun, F, and ΔHum were the dominant factors with higher independent contribution rates to ΔRHI between spring and summer at night, contributing 25.69%, 20.95%, and 18.16%, respectively. F (47.25%), ΔNDVI (14.07%), and ΔHum (13.60%) had a larger independent contribution rate to ΔRHI between the night of summer and autumn; ΔAir (28.21%), DEM (27.54%), and Δalbedo (11.99%) made larger independent contributions to ΔRHI between the night of autumn and winter; FL (21.27%), ΔSun (15.81%), and Δalbedo (15.23%) showed a strong ability to explain ΔRHI between the night of winter and spring.

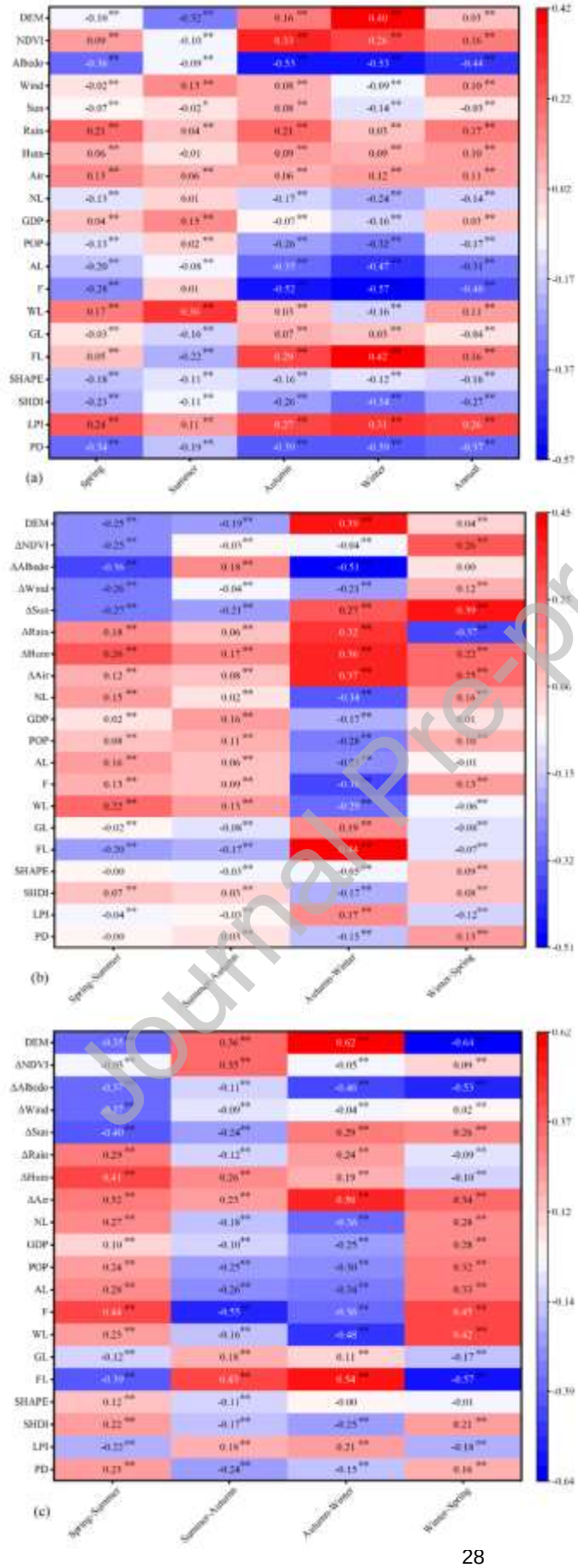

Fig. 8 Correlation matrix between time (seasons as well as day and night) inconsistency of RHI and influence factors.

Note: a represents the correlation matrix of time inconsistency of RHI between day and night, b represents the correlation matrix of the time inconsistency of RHI during daytime of different seasons, and c represents the correlation matrix of the time inconsistency of RHI during nighttime of different seasons. * meant $P < 0.05$, and ** meant $P < 0.01$.

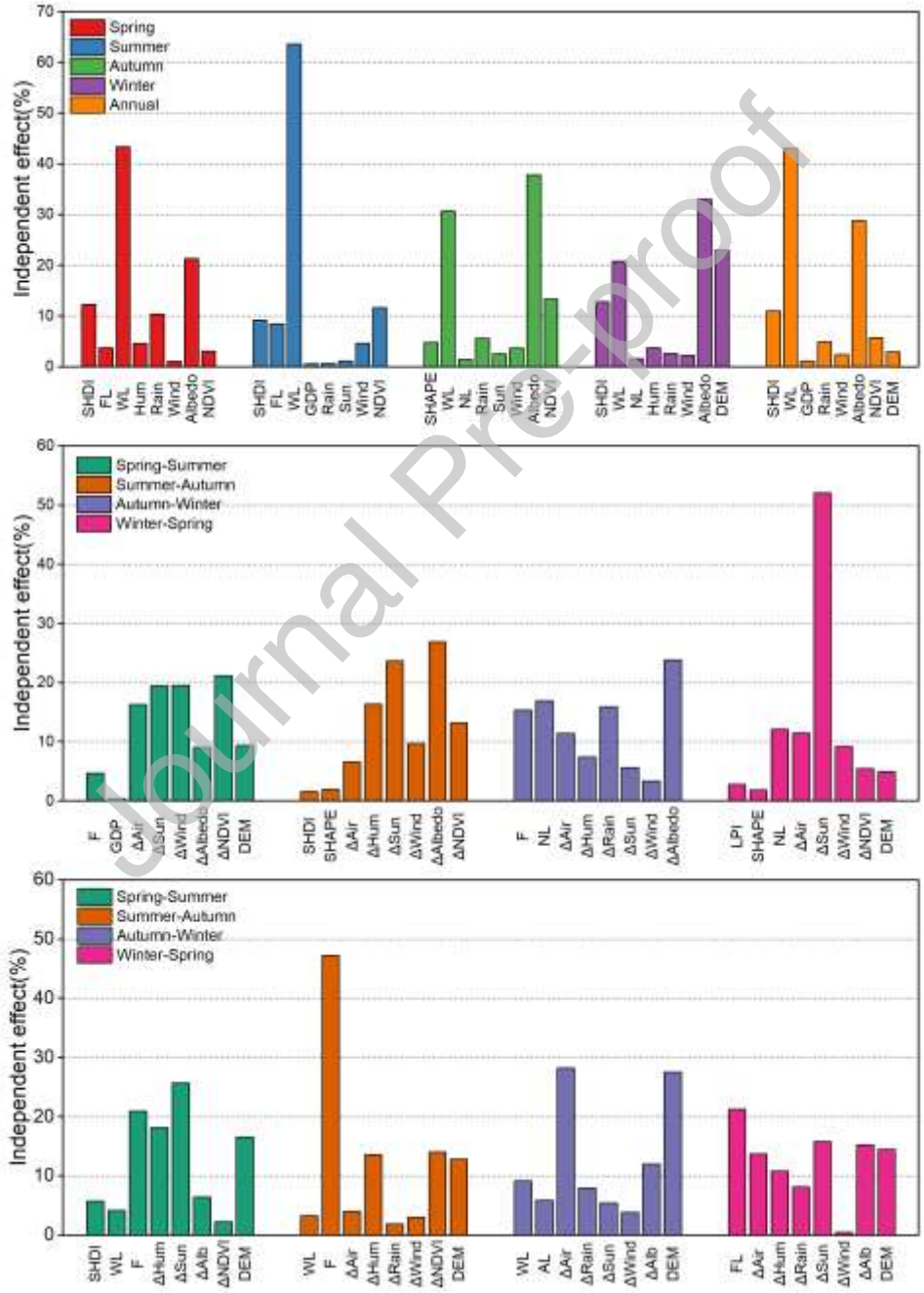

Fig. 9 Hierarchical partitioning analysis results for different time inconsistency.

Note: a represents the independent contribution rate of driving factor to time inconsistency between day and night; b represents the independent contribution rate of driving factor to time inconsistency between the day of seasons; c represents the independent contribution rate of driving factor to time inconsistency between the night of seasons.

4. Discussion

This study has contributed to research on UHI in several ways. First, an urban agglomeration, a form of spatial organization for the coordinated development of cities, emphasizes the connection between cities, and is one of the main trends in global development. We selected UAMRYR as an example, studied the spatial heterogeneity of LST and revealed the driving mechanism behind the time inconsistency of RHI. Second, a wide range of influencing factors from five layers were selected for a comprehensive investigation. Third, an independent and multi-factor interaction explanation on spatial heterogeneity of LST was detected without limitation of linear hypothesis and collinearity problems.

4.1 Seasonal variation of factors influencing on LST

Generally, the interpretation rate of the landscape composition and biophysical parameters layers were higher during the daytime of relatively high temperature seasons (spring, summer, and autumn) and annual. The climate conditions layer exhibited a higher interpretation rate during the daytime of winter, and the climate conditions layer and biophysical parameters layer could better explain LST at night comprehensively. Our results showed that landscape configuration on LST varied seasonally. The interpretation rate of PD, LPI, and SHDI in the landscape configuration was relatively stable in the season with higher temperature, while the of

SHAPE_MN in the entire year yielded a relatively weak interpretation rate. Compared with the landscape composition, the impact of landscape configuration on LST is limited, as previously reported (Chen et al., 2014; Li et al., 2017; Zhou et al., 2019). There were also significant seasonal variations in the landscape composition layer, and the overall trend appeared to increase from spring to summer and then fall to the lowest level in winter. During daytime of seasons with higher temperature and nighttime of summer, landscape composition had a relatively higher interpretation rate for LST compared to landscape configuration and climate conditions, whereas landscape composition in summer night could better explain the spatial variation of LST compared with summer day. Previous studies have shown that blue-green spaces reduced LST (Zhou et al., 2011). The forest land not only increases the latent heat flux through transpiration, thereby decreasing LST (Zhou et al., 2014), but also provides additional cooling by shading to block solar radiation. In this study, the proportion of forest land had a significant impact on LST in summer, which is consistent with the results of previous studies (Zhou et al., 2011; Zhou et al., 2014). The proportion of wetlands presented a relatively stable interpretation rate for LST during daytime, while during the nighttime of summer and autumn, the interpretation rate increased significantly. This was consistent with the results of certain studies (Hu et al., 2020), but incompatible with those of other studies (Peng et al., 2018), possibly owing to the number of wetlands in the study areas. The results of this study also showed that the proportion of forest land throughout summer could better explain the spatial heterogeneity of LST than the proportion of wetlands during nighttime, while the proportion of wetlands during the nighttime of spring, autumn, and annual had a stronger interpretation rate than forest land. This indicated that increasing the proportion of forest land during daytime of all seasons and nighttime of summer is one of the better effective ways of mitigating UHI compared with increasing the proportion of wetlands. The explanatory ability of the proportion of farmland was relatively higher during daytime of the higher temperature seasons because of the large extent of farmland and irrigation in UAMRYR (Yang et al., 2020). The

differences among various crops requiring water via irrigation probably result in the spatial heterogeneity of LST. The proportion of artificial land during the daytime of summer and annual showed robust capacity to explain LST variation, which was consistent with the inference made by previous studies stating that the higher the artificial land proportion, the stronger the effect of UHI in summer (Zhou et al., 2014; Peng et al., 2018). In seasons with relatively higher temperatures, the influence of the social economy layer on LST cannot be disregarded. The population could adequately explain the spatial variation of LST during the daytime of seasons with relatively higher temperature and annual, while GDP showed robust capacity to explain LST variations during nighttime of seasons with relatively higher temperatures, indicating that regulating population size and GDP structure may contribute to mitigating UHI (Li et al., 2020c). In contrast with previous studies, the interpretation rate of nighttime light was relatively low, because most previous studies describe UHI based on urban-rural differences rather than pixels with a great difference in nighttime light values between urban and rural areas. The interpretation rate of the climate conditions layer significantly influenced LST during daytime of winter, and the nighttime of spring, autumn, winter, and annual. Specifically, air temperature, air relative humidity, and rainfall showed robust capacity to explain the spatial heterogeneity of LST during the daytime of winter. The explanatory capacity of air temperature, air relative humidity, rainfall, and sunshine duration on LST variation was higher during the nighttime of spring and winter. The spatial variation of LST during the nighttime of annual can be adequately explained by air temperature, air relative humidity, and rainfall. Air temperature and LST were consistent, which may be because the long wave radiation released by the land surface affects the air temperature (Wang et al., 2020), and reducing air temperature and sunshine duration could decrease the evaporation of soil water (Yao et al., 2018). Rainfall is often accompanied by clouds blocking solar radiation, which mitigates LST, and other studies have shown that rainfall altered soil moisture: high rainfall could increase soil moisture, and low rainfall could negatively impact plants, thus affecting mitigation of vegetation on LST

(Yang et al., 2020). High wind speed can mitigate UHI by accelerating temperature exchange (Du et al., 2016; Zhou et al., 2018; Hu et al., 2019). High air relative humidity could also lead to low heat island intensity. The explanatory capacity of the biophysical parameters layer on LST varies seasonally. Except during the nighttime of winter, DEM had a higher interpretation rate of LST, which indicated that it was not beneficial to urban construction in the areas with higher DEM accompanied by lower intensity of human activities and higher vegetation coverage (Gong et al., 2011; Chen et al., 2012). The interpretation of NDVI showed a robust explanatory capacity in the relatively high temperature seasons (summer and autumn) and in the highest temperature season (summer), which was consistent with the results of previous studies (Peng et al., 2018). The albedo could well explain spatial variation of LST, which is owing to more low-reflective heat radiation to suppress UHI. Seasonal variations of driving forces on LST require various mitigation measures.

4.2 The driving mechanism of time inconsistency of RHI

This study showed that the ΔRHI between day and night was mainly attributable to the proportion of wetlands and albedo. UHI at night results from the surface heat flux generated during the daytime (Zhou et al., 2014), and albedo possibly influences the heat absorption capacity of the surface, resulting in time inconsistency of RHI between day and night. The specific heat capacity of the water body in the wetlands is larger and the cooling rate is slower, which may lead to the transformation of RHI between day and night.

ΔAlbedo showed robust capacity to explain the time inconsistency between the day of summer and autumn, autumn and winter by reflecting solar heat to relieve UHI (Deilami et al., 2018). ΔNDVI could explain the time inconsistency between the day of spring and summer, which indicated that the changes in NDVI represent one of the main ways of alleviating UHI. The explanatory capacity of ΔSun on ΔRHI between the day of summer and autumn, the day of winter and spring, the night of spring and

summer was higher. Sunshine duration affects the total amount of solar radiation, and solar radiation can promote UHI (Zhou et al., 2014), leading to time inconsistency between seasons. The proportion of farmland had a higher interpretation rate for ΔRHI between the night of spring and summer, summer and autumn, which may be due to soil water content and crop water content caused by differences in irrigation amount in the farm seasons (spring, summer, and autumn). ΔAir showed a robust capacity to explain time inconsistency between the night of autumn and winter, which was caused by the correlation between air temperature and LST. The proportion of forest land had a higher interpretation rate for ΔRHI between the night of winter and spring. In the winter, mitigation of LST because of deciduous trees was relatively weak, but during spring, mitigation of LST gradually increased, which influences the forest land proportion on ΔRHI between the night of winter and spring.

4.3 Implications for UHI mitigation

Our results confirm that NDVI, FL and WL can better explain LST in summer. However, there was a significant positive correlation between WL and ΔRHI among day and night, and WL promoted the time inconsistency of RHI, which indicated that WL might increase heat related risk and increase energy consumption during nighttime. Therefore, we suggest expanding urban green quantity, vigorously developing roof greening and vertical greening in the urban areas and accelerating the implementation of forest city development policy to alleviate urban heat island compared with increasing wetlands areas. Albedo also showed a strong explanation rate on LST, and a significant negative correlation with ΔRHI, which indicates that the application of high-albedo materials to reflect solar heat in urban construction, and the implementation of the new green building policy of modifying the thermal properties is also an effective measure to cool the city. In addition, the relative strong explanation rate of air relative humidity and rainfall during the daytime of winter, the nighttime of spring and winter indicates that UAMRYR should fully plan and reuse

rainwater, accelerate the implementation of "sponge city" strategy for UHI mitigation. There findings provide implications for the mitigation of UHI, and then promote sustainable land planning and society development.

4.4 Limitations

Our study has some limitations. First, this study used data dated back to 2010, when the development of urbanization in China has aggravated UHI to a certain extent; however, with the continuous promotion of ventilation corridors, urban parks, ecological green wedges, and vertical greening policies in urban areas, UHI might have been alleviated to a certain extent. Therefore, the phenomenon of UHI still exists and limitation of data has a little effect on the results of this study.

There were other uncertainties in this study due to data limitations. For example, the accuracy of meteorological data depended on the distribution density of meteorological stations, and anthropogenic heat emissions and three-dimensional data (sky view factor, surface roughness) were not taken into account. In addition, it is essential to optimize the number of influence factors in HP to at least nine. These limitations should be addressed in further studies.

5. Conclusions

Urban heat island could result in environmental, energy, and health problems and these issues have greatly limited sustainable development of cities and society. Adverse effects of UHI have become urgent matters in urban ecology. This study overcame some limitations in previous studies, including the restraint of linear hypotheses, the deficiency of the interactive effect between influencing factors on LST, the problem of collinearity, and the insufficiency of urban agglomeration research. We selected geo-detector method to solve above problems and quantified the influence of different layer factors and their interaction on LST. In addition, we used

Spearman correlation, OLS regression, all-subset regression, and HP analysis to reveal the driving mechanism of time inconsistency of RHI. The result of the geo-detector showed seasonal variations in the dominant factor affecting LST spatial heterogeneity. The dominant factors affecting LST spatial heterogeneity in the hotter seasons (spring, summer, and autumn) were found to be the landscape composition layer and biophysical parameters layer with a higher contribution rate. During the daytime of winter, the dominant factors were the climate conditions layer, and the climate conditions layer and biophysical parameters layer dominated during nighttime. The proportions of wetlands and albedo greatly influenced the ΔRHI between day and night. The dominant factors of ΔRHI between the day of seasons (spring–summer, summer–autumn, autumn–winter, and winter–spring) were ΔNDVI, Δalbedo, Δalbedo, and ΔSun, respectively. ΔSun, F, ΔAir, and FL were the dominant factors of ΔRHI between night of seasons. Increasing urban green quantity and popularization of high-albedo materials are effective measures for UHI mitigation. The findings in this study recommend various mitigation strategies for city planners and policy makers to make rational and scientifically sound decisions, and promote environmental sustainability.

References

Ali, J. M., Marsh, S. H., & Smith, M. J. (2016). Modelling the spatiotemporal change of canopy urban heat islands. *Building and Environment*, *107*, 64–78. https://doi.org/10.1016/j.buildenv.2016.07.010

Arifwidodo, S. D., & Chandrasiri, O. (2020). Urban heat stress and human health in Bangkok, Thailand. *Environmental Research*, *185*(March), 109398. https://doi.org/10.1016/j.envres.2020.109398

Azhdari, A., Soltani, A., & Alidadi, M. (2018). Urban morphology and landscape

structure effect on land surface temperature: Evidence from Shiraz, a semi-arid city. *Sustainable Cities and Society*, *41*(March), 853–864. https://doi.org/10.1016/j.scs.2018.06.034

Bai, L., Jiang, L., Yang, D. yang, & Liu, Y. bin. (2019). Quantifying the spatial heterogeneity influences of natural and socioeconomic factors and their interactions on air pollution using the geographical detector method: A case study of the Yangtze River Economic Belt, China. *Journal of Cleaner Production*, *232*, 692–704. https://doi.org/10.1016/j.jclepro.2019.05.342

Cao, F., Ge, Y., & Wang, J. F. (2013). Optimal discretization for geographical detectors-based risk assessment. *GIScience and Remote Sensing*, *50*(1), 78–92. https://doi.org/10.1080/15481603.2013.778562

Chen, Z., Gong, C., Wu, J., & Yu, S. (2012). The influence of socioeconomic and topographic factors on nocturnal urban heat islands: A case study in Shenzhen, China. *International Journal of Remote Sensing*, *33*(12), 3834–3849. https://doi.org/10.1080/01431161.2011.635717

Chen, A., Yao, L., Sun, R., & Chen, L. (2014). How many metrics are required to identify the effects of the landscape pattern on land surface temperature? *Ecological Indicators*, *45*, 424–433. https://doi.org/10.1016/j.ecolind.2014.05.002

Chen, W., Ye, X., Li, J., Fan, X., Liu, Q., & Dong, W. (2019). Analyzing requisition–compensation balance of farmland policy in China through telecoupling: A case study in the middle reaches of Yangtze River Urban Agglomerations. *Land Use*

Policy, *83*(October 2018), 134–146. https://doi.org/10.1016/j.landusepol.2019.01.031

Chen, T., Feng, Z., Zhao, H., & Wu, K. (2020). Identification of ecosystem service bundles and driving factors in Beijing and its surrounding areas. *Science of the Total Environment*, *711*, 134687. https://doi.org/10.1016/j.scitotenv.2019.134687

Cui, Y., Xu, X., Dong, J., & Qin, Y. (2016). Influence of urbanization factors on surface urban heat island intensity: A comparison of countries at different developmental phases. *Sustainability (Switzerland)*, *8*(8). https://doi.org/10.3390/su8080706

Dai, X., Wang, L., Huang, C., Fang, L., Wang, S., & Wang, L. (2020). Spatio-temporal variations of ecosystem services in the urban agglomerations in the middle reaches of the Yangtze River, China. *Ecological Indicators*, *115*(January), 106394. https://doi.org/10.1016/j.ecolind.2020.106394

Deilami, K., Kamruzzaman, M., & Liu, Y. (2018). Urban heat island effect: A systematic review of spatio-temporal factors, data, methods, and mitigation measures. *International Journal of Applied Earth Observation and Geoinformation*, *67*(September 2017), 30–42. https://doi.org/10.1016/j.jag.2017.12.009

Diem, J. E., Stauber, C. E., & Rothenberg, R. (2017). Heat in the southeastern United States: Characteristics, trends, and potential health impact. *PLoS ONE*, *12*(5), 1–19. https://doi.org/10.1371/journal.pone.0177937

Du, H., Wang, D., Wang, Y., Zhao, X., Qin, F., Jiang, H., & Cai, Y. (2016).

Influences of land cover types, meteorological conditions, anthropogenic heat and urban area on surface urban heat island in the Yangtze River Delta Urban Agglomeration. *Science of the Total Environment*, *571*, 461–470. https://doi.org/10.1016/j.scitotenv.2016.07.012

Duan, Q., & Tan, M. (2020). Using a geographical detector to identify the key factors that influence urban forest spatial differences within China. *Urban Forestry and Urban Greening*, *49*(January), 126623. https://doi.org/10.1016/j.ufug.2020.126623

Estoque, R. C., Murayama, Y., & Myint, S. W. (2017). Effects of landscape composition and pattern on land surface temperature: An urban heat island study in the megacities of Southeast Asia. *Science of the Total Environment*, *577*, 349–359. https://doi.org/10.1016/j.scitotenv.2016.10.195

Firozjaei, M. K., Fathololoumi, S., Kiavarz, M., Arsanjani, J. J., & Alavipanah, S. K. (2020). Modelling surface heat island intensity according to differences of biophysical characteristics: A case study of Amol city, Iran. *Ecological Indicators*, *109*(October 2019), 105816. https://doi.org/10.1016/j.ecolind.2019.105816

Firozjaei, M. K., Kiavarz, M., Alavipanah, S. K., Lakes, T., & Qureshi, S. (2018). Monitoring and forecasting heat island intensity through multi-temporal image analysis and cellular automata-Markov chain modelling: A case of Babol city, Iran. *Ecological Indicators*, *91*(July 2017), 155–170. https://doi.org/10.1016/j.ecolind.2018.03.052

Gong, C., Chen, J., & Yu, S. (2011). Spatiotemporal dynamics of urban forest conversion through model urbanization in Shenzhen, China. *International Journal of Remote Sensing*, *32*(24), 9071–9092.

https://doi.org/10.1080/01431161.2010.549848

Greene, C. S., & Kedron, P. J. (2018). Beyond fractional coverage: A multilevel approach to analyzing the impact of urban tree canopy structure on surface urban heat islands. *Applied Geography*, *95*(February 2017), 45–53. https://doi.org/10.1016/j.apgeog.2018.04.004

Guo, G., Wu, Z., Xiao, R., Chen, Y., Liu, X., & Zhang, X. (2015). Impacts of urban biophysical composition on land surface temperature in urban heat island clusters. *Landscape and Urban Planning*, *135*, 1–10. https://doi.org/10.1016/j.landurbplan.2014.11.007

Heaviside, C., Vardoulakis, S., & Cai, X. M. (2016). Attribution of mortality to the urban heat island during heatwaves in the West Midlands, UK. *Environmental Health: A Global Access Science Source*, *15*(Suppl 1). https://doi.org/10.1186/s12940-016-0100-9

Hirano, Y., & Fujita, T. (2012). Evaluation of the impact of the urban heat island on residential and commercial energy consumption in Tokyo. *Energy*, *37*(1), 371–383. https://doi.org/10.1016/j.energy.2011.11.018

Hu, Y., Hou, M., Jia, G., Zhao, C., Zhen, X., & Xu, Y. (2019). Comparison of surface and canopy urban heat islands within megacities of eastern China. *ISPRS Journal of Photogrammetry and Remote Sensing*, *156*(March), 160–168. https://doi.org/10.1016/j.isprsjprs.2019.08.012

Hu, D., Meng, Q., Zhang, L., & Zhang, Y. (2020). Spatial quantitative analysis of the potential driving factors of land surface temperature in different “Centers” of

polycentric cities: A case study in Tianjin, China. *Science of the Total Environment*, *706*, 135244. https://doi.org/10.1016/j.scitotenv.2019.135244

Jamei, Y., Rajagopalan, P., & Sun, Q. (Chayn). (2019). Spatial structure of surface urban heat island and its relationship with vegetation and built-up areas in Melbourne, Australia. *Science of the Total Environment*, *659*, 1335–1351. https://doi.org/10.1016/j.scitotenv.2018.12.308

Kotharkar, R., Bagade, A., & Ramesh, A. (2019). Assessing urban drivers of canopy layer urban heat island: A numerical modeling approach. *Landscape and Urban Planning*, *190*(May), 103586. https://doi.org/10.1016/j.landurbplan.2019.05.017

Li, J.X., Song, C., Cao, L., Zhu, F., Meng, X., & Wu, J. (2011). Impacts of landscape structure on surface urban heat islands: A case study of Shanghai, China. *Remote Sensing of Environment*, *115*(12), 3249–3263. https://doi.org/10.1016/j.rse.2011.07.008

Li, W., Cao, Q., Lang, K., & Wu, J. (2017). Linking potential heat source and sink to urban heat island: Heterogeneous effects of landscape pattern on land surface temperature. *Science of the Total Environment*, *586*, 457–465. https://doi.org/10.1016/j.scitotenv.2017.01.191

Li, J.F., Wang, F., Fu, Y., Guo, B., Zhao, Y., & Yu, H. (2020a). A Novel SUHI Referenced Estimation Method for Multicenters Urban Agglomeration using DMSP/OLS Nighttime Light Data. *IEEE Journal of Selected Topics in Applied Earth Observations and Remote Sensing*, *13*, 1416–1425. https://doi.org/10.1109/JSTARS.2020.2981285

Li, L., Zha, Y., & Zhang, J. (2020b). Spatially non-stationary effect of underlying driving factors on surface urban heat islands in global major cities. *International Journal of Applied Earth Observation and Geoinformation*, *90*(April), 102131. https://doi.org/10.1016/j.jag.2020.102131

Li, Y., Sun, Y., Li, J., & Gao, C. (2020c). Socioeconomic drivers of urban heat island effect: Empirical evidence from major Chinese cities. *Sustainable Cities and Society*, *63*(April), 102425. https://doi.org/10.1016/j.scs.2020.102425

Liu, X., Zhou, Y., Yue, W., Li, X., Liu, Y., & Lu, D. (2020). Spatiotemporal patterns of summer urban heat island in Beijing, China using an improved land surface temperature. *Journal of Cleaner Production*, *257*, 120529. https://doi.org/10.1016/j.jclepro.2020.120529

Macintyre, H. L., Heaviside, C., Cai, X., & Phalkey, R. (2021). The winter urban heat island: Impacts on cold-related mortality in a highly urbanized European region for present and future climate. *Environment International*, *154*(January), 106530. https://doi.org/10.1016/j.envint.2021.106530

Manoli, G., Fatichi, S., Schläpfer, M., Yu, K., Crowther, T. W., Meili, N., Burlando, P., Katul, G. G., & Bou-Zeid, E. (2019). Magnitude of urban heat islands largely explained by climate and population. *Nature*, *573*(7772), 55–60. https://doi.org/10.1038/s41586-019-1512-9

Mathew, A., Khandelwal, S., & Kaul, N. (2016). Spatial and temporal variations of urban heat island effect and the effect of percentage impervious surface area and elevation on land surface temperature: Study of Chandigarh city, India. *Sustainable Cities and Society*, *26*, 264–277. https://doi.org/10.1016/j.scs.2016.06.018

Oke, T. R. (1976). The distinction between canopy and boundary-layer urban heat Islands. *Atmosphere*, *14*(4), 268–277. https://doi.org/10.1080/00046973.1976.9648422

Oke T R. (1982). The energetic basis of the urban heat island. *Quarterly Journal of the Royal Meteorological Society*, 108(455): 1-24. https://doi.org/10.1002/qj.49710845502

Patz, J. A., Campbell-Lendrum, D., Holloway, T., & Foley, J. A. (2005). Impact of regional climate change on human health. *Nature*, *438*(7066), 310–317. https://doi.org/10.1038/nature04188

Peng, S., Piao, S., Ciais, P., Friedlingstein, P., Ottle, C., Bréon, F. M., Nan, H., Zhou, L., & Myneni, R. B. (2012). Surface urban heat island across 419 global big cities. *Environmental Science and Technology*, *46*(2), 696–703. https://doi.org/10.1021/es2030438

Peng, J., Chen, S., Lü, H., Liu, Y., & Wu, J. (2016). Spatiotemporal patterns of remotely sensed PM2.5 concentration in China from 1999 to 2011. *Remote Sensing of Environment*, *174*, 109–121. https://doi.org/10.1016/j.rse.2015.12.008

Peng, J., Jia, J., Liu, Y., Li, H., & Wu, J. (2018). Seasonal contrast of the dominant factors for spatial distribution of land surface temperature in urban areas. *Remote Sensing of Environment*, *215*(April 2017), 255–267. https://doi.org/10.1016/j.rse.2018.06.010

Santamouris, M. (2013). Using cool pavements as a mitigation strategy to fight urban heat island - A review of the actual developments. *Renewable and Sustainable Energy Reviews*, *26*, 224–240. https://doi.org/10.1016/j.rser.2013.05.047

Shi, T., Hu, Z., Shi, Z., Guo, L., Chen, Y., Li, Q., & Wu, G. (2018a). Geo-detection of

factors controlling spatial patterns of heavy metals in urban topsoil using multi-source data. *Science of the Total Environment*, *643*, 451–459. https://doi.org/10.1016/j.scitotenv.2018.06.224

Shi, Y., Matsunaga, T., Yamaguchi, Y., Li, Z., Gu, X., & Chen, X. (2018b). Long-term trends and spatial patterns of satellite-retrieved PM2.5 concentrations in South and Southeast Asia from 1999 to 2014. *Science of the Total Environment*, *615*, 177–186. https://doi.org/10.1016/j.scitotenv.2017.09.241

Stathopoulou, E., Mihalakakou, G., Santamouris, M., & Bagiorgas, H. S. (2008). On the impact of temperature on tropospheric Ozone concentration levels in urban environments. *Journal of Earth System Science*, *117*(3), 227–236. https://doi.org/10.1007/s12040-008-0027-9

Stewart, I. D., & Oke, T. R. (2012). Local climate zones for urban temperature studies. *Bulletin of the American Meteorological Society*, *93*(12), 1879–1900. https://doi.org/10.1175/BAMS-D-11-00019.1

Stewart, I. D., Oke, T. R., Bechtel, B., Foley, M. M., Mills, G., Ching, J., See, L., Alexander, P. J., O'Connor, M., Albuquerque, T., Andrade, M. de F., Brovelli, M., Debashish, D., Fonte, C. C., Petit, G., Hanif, U., Jimenez, J., Lackner, S., Weibo, L., … Ce, D. (2015). Generating WUDAPT's Specific Scale -dependent Urban Modeling and Activity Parameters: Collection of Level 1 and Level 2 Data. *ICUC9, Toulouse, France (20-24 July)*, *5*(4), 1–4. http://www.sciencedirect.com/science/article/pii/0004698173901406%5Cnhttp://sciencedomain.org/abstract/9606%5Cnhttp://www.sciencedirect.com/science/article/pii/S1878029614001340%5Cnhttp://ieeexplore.ieee.org/lpdocs/epic03/wrapp

er.htm?arnumber=7120456

Sun, Y., & Augenbroe, G. (2014). Urban heat island effect on energy application studies of office buildings. *Energy and Buildings*, *77*, 171–179. https://doi.org/10.1016/j.enbuild.2014.03.055

Tan, J., Zheng, Y., Tang, X., Guo, C., Li, L., Song, G., Zhen, X., Yuan, D., Kalkstein, A. J., Li, F., & Chen, H. (2010). The urban heat island and its impact on heat waves and human health in Shanghai. *International Journal of Biometeorology*, *54*(1), 75–84. https://doi.org/10.1007/s00484-009-0256-x

Tong, H., Walton, A., Sang, J., & Chan, J. C. L. (2005). Numerical simulation of the urban boundary layer over the complex terrain of Hong Kong. *Atmospheric Environment*, *39*(19), 3549–3563. https://doi.org/10.1016/j.atmosenv.2005.02.045

Voogt, J. A., & Oke, T. R. (2003). Thermal remote sensing of urban climates. *Remote Sensing of Environment*, *86*(3), 370–384. https://doi.org/10.1016/S0034-4257(03)00079-8

Wang, J. F., Li, X. H., Christakos, G., Liao, Y. L., Zhang, T., Gu, X., & Zheng, X. Y. (2010). Geographical detectors-based health risk assessment and its application in the neural tube defects study of the Heshun Region, China. *International Journal of Geographical Information Science*, *24*(1), 107–127. https://doi.org/10.1080/13658810802443457

Wang J. F., Xu C, D., (2017). Geographic probe: principle and prospect. *Acta Geographica Sinica*. 72, 116-134.

Wang, L., & Chen, L. (2018a). Analysis: The impact of new transportation modes on population distribution in Jing-Jin-Ji region of China. *Scientific Data*, *5*(388), 1–15. https://doi.org/10.1038/sdata.2017.204

Wang, H., Wu, Q., Hu, W., Huang, B., Dong, L., & Liu, G. (2018b). Using multi-medium factors analysis to assess heavy metal health risks along the Yangtze River in Nanjing, Southeast China. *Environmental Pollution*, *243*, 1047–1056. https://doi.org/10.1016/j.envpol.2018.09.036

Wang, L., & Li, D. (2019). Modulation of the urban boundary-layer heat budget by a heatwave. *Quarterly Journal of the Royal Meteorological Society*, *145*(722), 1814–1831. https://doi.org/10.1002/qj.3526

Wang, W., Yao, X., & Shu, J. (2020). Air advection induced differences between canopy and surface heat islands. *Science of the Total Environment*, *725*, 138120. https://doi.org/10.1016/j.scitotenv.2020.138120

Yadav, N., Sharma, C., Peshin, S. K., & Masiwal, R. (2017). Study of intra-city urban heat island intensity and its influence on atmospheric chemistry and energy consumption in Delhi. *Sustainable Cities and Society*, *32*(January), 202–211. https://doi.org/10.1016/j.scs.2017.04.003

Yang, Q., Huang, X., & Li, J. (2017). Assessing the relationship between surface urban heat islands and landscape patterns across climatic zones in China. *Scientific Reports*, *7*(1), 1–11. https://doi.org/10.1038/s41598-017-09628-w

Yang, Z., Chen, Y., Wu, Z., Qian, Q., Zheng, Z., & Huang, Q. (2019). Spatial heterogeneity of the thermal environment based on the urban expansion of natural cities using open data in Guangzhou, China. *Ecological Indicators*, *104*(May), 524–534. https://doi.org/10.1016/j.ecolind.2019.05.032

Yang, Q., Huang, X., & Tang, Q. (2020). Irrigation cooling effect on land surface temperature across China based on satellite observations. *Science of the Total Environment*, *705*, 135984. https://doi.org/10.1016/j.scitotenv.2019.135984

Yao, R., Wang, L., Huang, X., Zhang, W., Li, J., & Niu, Z. (2018). Interannual variations in surface urban heat island intensity and associated drivers in China. *Journal of Environmental Management*, *222*(January), 86–94. https://doi.org/10.1016/j.jenvman.2018.05.024

Yu, Z. W., Yao, Y., Yang, G., Wang, X., & Vejre, H. (2019). Spatiotemporal patterns and characteristics of remotely sensed region heat islands during the rapid urbanization (1995–2015) of Southern China. *Science of the Total Environment*, *674*, 242–254. https://doi.org/10.1016/j.scitotenv.2019.04.088

Yuan, J., Bian, Z., Yan, Q., Gu, Z. Y., & Yu, H. C. (2020). An approach to the temporal and spatial characteristics of vegetation in the growing season in Western China. *Remote Sensing*, *12*(6). https://doi.org/10.3390/rs12060945

Zhang, Q., & Seto, K. C. (2011). Mapping urbanization dynamics at regional and global scales using multi-temporal DMSP/OLS nighttime light data. *Remote Sensing of Environment*, *115*(9), 2320–2329. https://doi.org/10.1016/j.rse.2011.04.032

Zhang, Y., Balzter, H., Zou, C., Xu, H., & Tang, F. (2015). Characterizing bi-temporal patterns of land surface temperature using landscape metrics based on sub-pixel classifications from Landsat TM/ETM+. *International Journal of Applied Earth Observation and Geoinformation*, *42*, 87–96. https://doi.org/10.1016/j.jag.2015.06.007

Zhao, J., Zhao, X., Liang, S., Zhou, T., Du, X., Xu, P., & Wu, D. (2020). Assessing the thermal contributions of urban land cover types. *Landscape and Urban Planning*, *204*(19), 103927. https://doi.org/10.1016/j.landurbplan.2020.103927

Zhong, S., Qian, Y., Zhao, C., Leung, R., Wang, H., Yang, B., Fan, J., Yan, H., Yang, X. Q., & Liu, D. (2017). Urbanization-induced urban heat island and aerosol effects on climate extremes in the Yangtze River Delta region of China. *Atmospheric Chemistry and Physics*, *17*(8), 5439–5457. https://doi.org/10.5194/acp-17-5439-2017

Zhou, W., Huang, G., & Cadenasso, M. L. (2011). Does spatial configuration matter? Understanding the effects of land cover pattern on land surface temperature in urban landscapes. *Landscape and Urban Planning*, *102*(1), 54–63. https://doi.org/10.1016/j.landurbplan.2011.03.009

Zhou, D., Zhao, S., Liu, S., Zhang, L., & Zhu, C. (2014). Surface urban heat island in China's 32 major cities: Spatial patterns and drivers. *Remote Sensing of Environment*, *152*, 51–61. https://doi.org/10.1016/j.rse.2014.05.017

Zhou, D., Bonafoni, S., Zhang, L., & Wang, R. (2018). Remote sensing of the urban heat island effect in a highly populated urban agglomeration area in East China. *Science of the Total Environment*, *628–629*(219), 415–429. https://doi.org/10.1016/j.scitotenv.2018.02.074

Zhou, D., Xiao, J., Bonafoni, S., Berger, C., Deilami, K., Zhou, Y., Frolking, S., Yao, R., Qiao, Z., & Sobrino, J. A. (2019). Satellite remote sensing of surface urban heat islands: Progress, challenges, and perspectives. *Remote Sensing*, *11*(1), 1–36. https://doi.org/10.3390/rs11010048

Zhu, Z., Wang, J., Hu, M., & Jia, L. (2019). Geographical detection of groundwater pollution vulnerability and hazard in karst areas of Guangxi Province, China.

Environmental Pollution, *245*, 627–633.

https://doi.org/10.1016/j.envpol.2018.10.017

Appendices

Table A.1 Influencing factors selected from previous studies.

Categories of variables	Variables	Sources
Landscape configuration	PD	Chen et al., 2014; Zhang et al., 2015; Estoque et al., 2017; Li et al., 2017; Yang et al., 2017; Peng et al., 2018
	LPI	Estoque et al., 2017; Li et al., 2017; Peng et al., 2018;
	SHDI	Chen et al., 2014; Li et al., 2017; Yang et al., 2017; Azhdari et al., 2018; Peng et al., 2018
	SHAPE	Li et al., 2017; Estoque et al., 2017
Landscape composition	FL GL WL F AL	Li et al., 2011; Chen et al., 2014; Li et al., 2017; Yang et al., 2017; Deilami et al., 2018; Peng et al.; 2018

Social economy	POP	Deilami et al., 2018; Yao et al., 2018; Manoli et al., 2019; Li et al., 2020c
	GDP	Cui et al., 2016; Li et al., 2020c
	NL	Peng et al., 2012; Zhou et al., 2014; Li et al., 2020b; Hu et al., 2020
Climate conditions	Air	Peng et al., 2012; Du et al., 2016; Deilami et al., 2018; Zhou et al., 2018; Yao et al., 2018; Hu et al., 2019
	Hum	Hu et al., 2019
	Rain	Du et al., 2016; Yao et al., 2018; Zhou et al., 2018; Manoli et al., 2019; Hu et al., 2019
	Sun	Yao et al., 2018
	Wind	Du et al., 2016; Yao et al., 2018; Zhou et al., 2018; Zhou et al., 2019; Wang et al., 2020
Biophysical parameters	Albedo	Peng et al., 2012; Santamouris et al., 2013; Zhou et al., 2014; Li et al., 2018; Deilami et al., 2018; Yao et al., 2018; Zhou et al., 2018; Kotharkar et al., 2019; Manoli et al., 2019; Zhou et al., 2019; Li et al., 2020b
	NDVI	Li et al., 2011; Chen et al., 2014; Guo et al., 2015; Azhdari et al., 2018; Deilami et al., 2018; Peng et al., 2018; Wang et al., 2018c; Jamei et al., 2019; Zhou et al., 2019; Li et al., 2020b; Hu et al., 2020; Li et al., 2020c
	DEM	Chen et al., 2012; Wang et al., 2018c; Li et al., 2020a

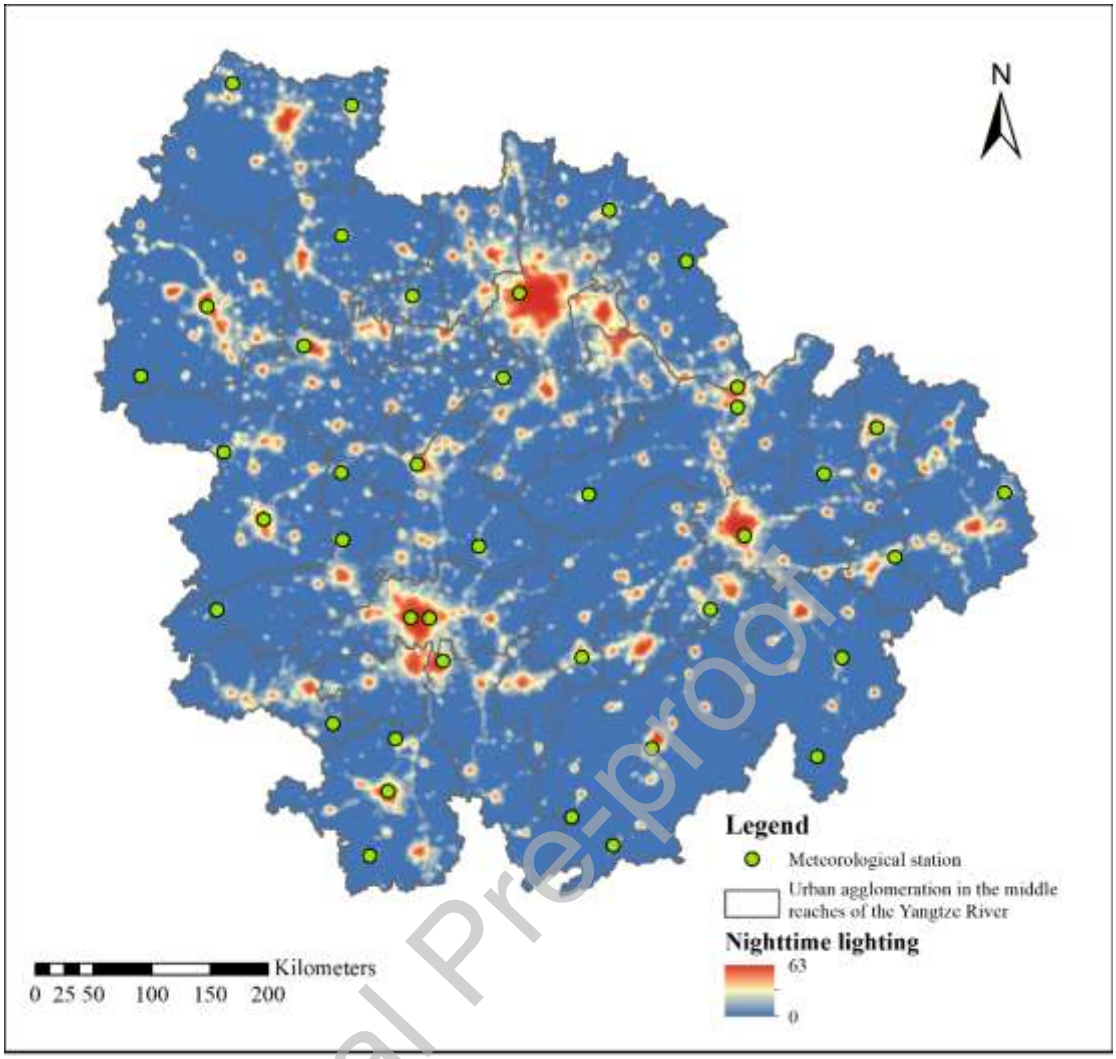

Fig A.1 Distribution of meteorological stations and nighttime lighting.

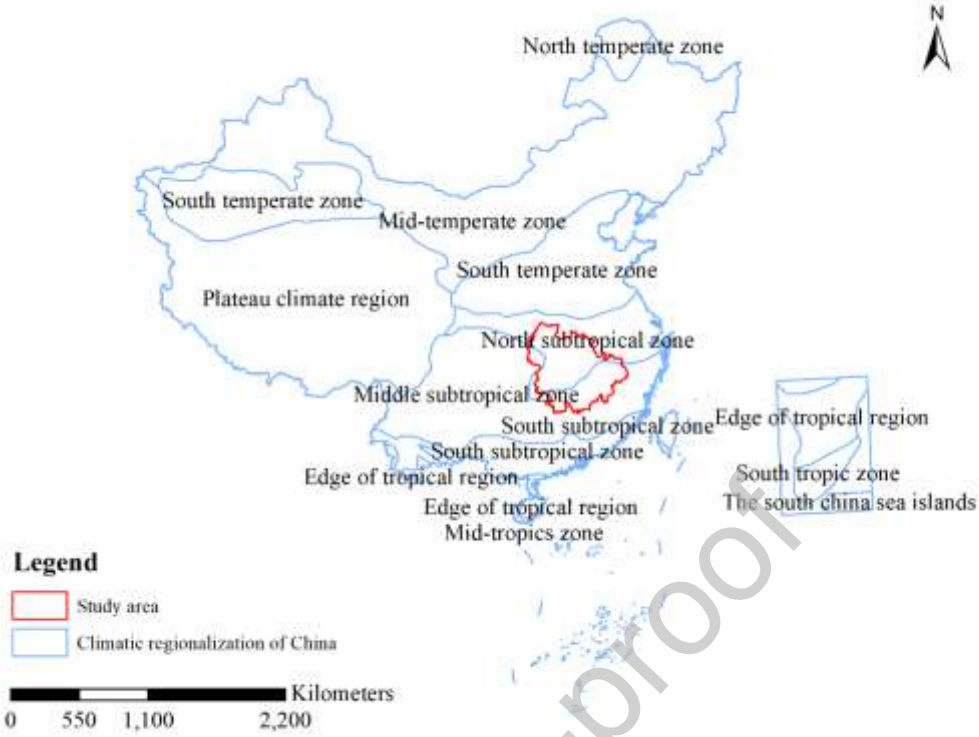

Fig A.2 Classification of the climate regionalization in China.

Table A.2 Classification of regional heat island.

RHI level	Range of LST
Low	$T_S \leq T_{mean}$ - 1.5std
Sub-low	T_{mean} - 1.5std < $T_S \leq T_{mean}$ - 0.5std
Medium	T_{mean} - 0.5std < $T_S \leq T_{mean}$ + 0.5std
Sub-high	T_{mean} + 0.5std < $T_S \leq T_{mean}$ + 1.5std
High	$T_S > T_{mean}$ + 1.5std

Note: “mean” and “std” represent the average value and standard deviation of LST in study area, respectively.

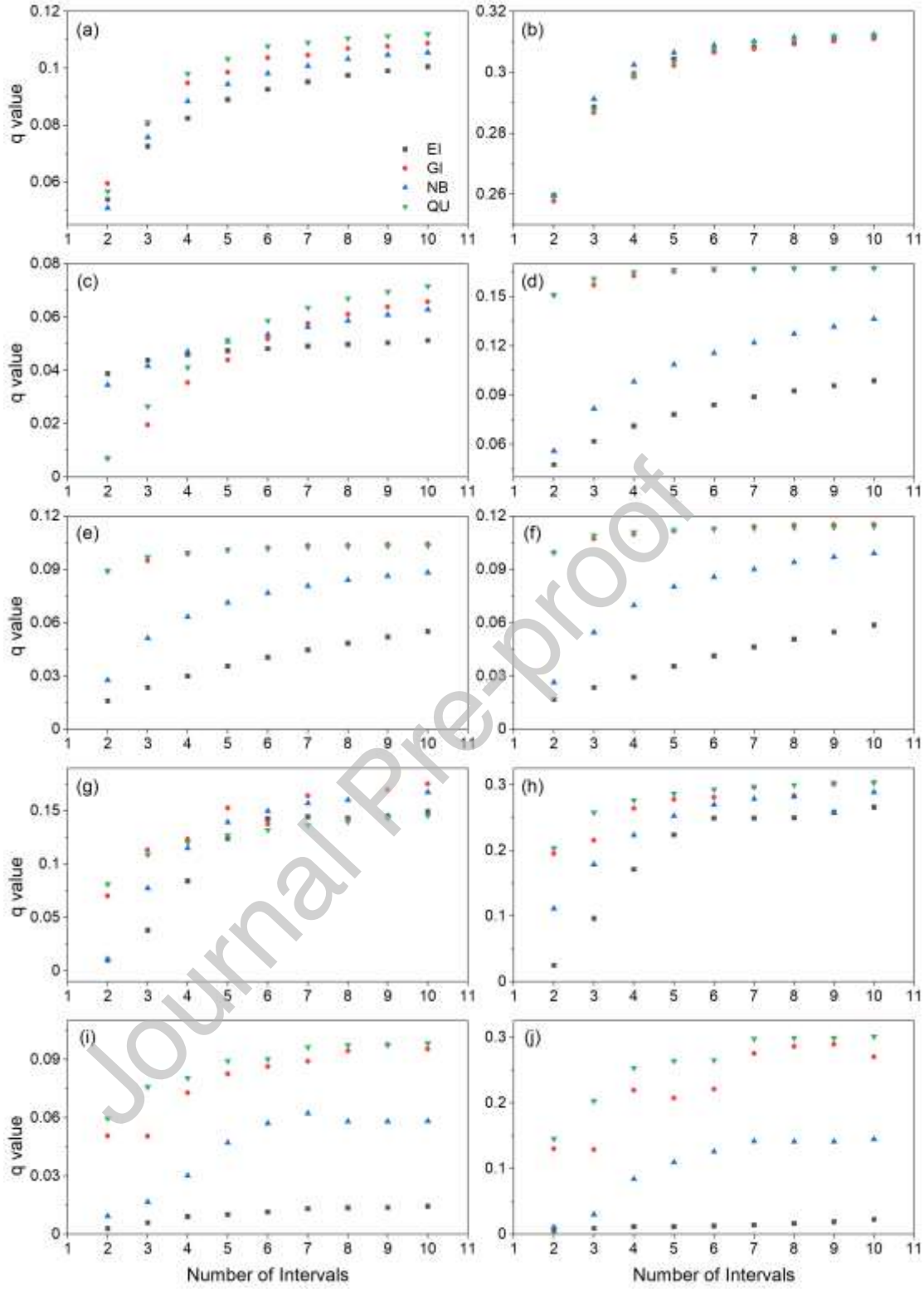

Fig A.3 Map of PD values for five impact factors divided into a range of 2–10 intervals using the four discretization methods.

Note: a, c, e, g and i, representing the proportion of forest land, the proportion of wetlands, the proportion of artificial land, NDVI and GDP, is q value in the daytime,

respectively; b, d, f, h and j, representing the proportion of forest land, the proportion of wetlands, the proportion of artificial land, NDVI and GDP, is q value in the nighttime.

Table A.3 The all-subset regression model for time inconsistency of RHI between day and night in different seasons.

Time	Model	Adj R^2
Spring	Y=16.6644 - 0.8967*SHDI - 0.0069*FL+0.0318*WL - 0.1630*Hum + 0.0075*Rain - 1.2287*Wind - 33.3615*albedo + 2.0498*NDVI	0.49
Summer	Y=-3.7823 - 0.5421*SHDI - 0.0061*FL + 0.0374*WL + 0.0001*GDP + 0.0027*Rain - 0.007*Sun + 1.6063*Wind + 2.7916*NDVI	0.39
Autumn	Y=-3.4998 - 0.6644*SHAPE + 0.0362*WL + 0.0211NL + 0.0085*Rain + 0.0153*Sun + 1.1289*Wind - 26.1252*albedo + 4.6441*NDVI	0.56
Winter	Y= -5.7956 - 0.6566*SHDI + 0.0264*WL + 0.0191*NL + 0.0872*Hum -0.0324*Rain + 1.4894*Wind - 25.2959*albedo + 0.0014*DEM	0.52
Annual	Y=-0.2627 -0.6695*SHDI + 0.0371*WL + 0.0001*GDP + 0.0033*Rain + 1.0152*Wind - 22.5889*Albedo + 1.4545*NDVI + 0.0003*DEM	0.52

Table A.4 The all-subset regression model for time inconsistency of RHI between different seasons in the daytime.

Time	Model	Adj R^2
Spring-Summer	Y= 7.3574 + 0.0022*F - 0.5814*ΔAir - 0.0106*ΔSun - 2.1979*ΔWind+ 3.1634*Δalbedo - 3.0305*ΔNDVI - 0.0006*DEM	0.27

Summer-Autumn	Y= -1.2104* - 0.1462*SHDI - 0.1766*SHAPE - 0.1715*ΔAir + 0.0611*ΔHum - 0.0093*ΔSun + 1.5820*ΔWind + 14.8510*Δalbedo - 2.5345*ΔNDVI	0.14
Autumn-Winter	Y= 0.3830 - 0.0044*F - 0.0203*NL + 0.2032*ΔAir + 0.0328*ΔHum + 0.0118*ΔRain - 0.0557*ΔSun + 1.7403*ΔWind - 10.7049*Δalbedo	0.36
Winter-Spring	Y= 1.5357 - 0.0025*LPI + 0.2067*SHAPE+ 0.0168*NL - 0.3495*ΔAir + 0.0440*ΔSun + 3.0707*ΔWind - 0.7810*ΔNDVI+0.0004*DEM	0.27

Table A.5 The all-subset regression model for time inconsistency of RHI between different seasons in the nighttime.

Time	Model	Adj R2
Spring-Summer	Y=3.2438 + 0.2635*SHDI - 0.0108*WL + 0.0065*F - 0.1536*ΔHum - 0.0417*ΔSun - 8.3154*Δalbedo - 1.6709*ΔNDVI - 0.0010*DEM	0.43
Summer-Autumn	Y=-1.0497 + 0.0061*WL - 0.0123*F - 0.1742*ΔAir + 0.1402*ΔHum - 0.0024*ΔRain + 2.0648*ΔWind + 1.2016*ΔNDVI + 0.0005*DEM	0.38
Autumn-Winter	Y=5.6308 - 0.0063*WL - 0.0118*AL + 0.7126*ΔAir + 0.0161*ΔRain - 0.0587*ΔSun + 2.7144*ΔWind - 5.2790*Δalbedo + 0.0011*DEM	0.53
Winter-Spring	Y=-7.2814 - 0.0065*FL + 0.5594*ΔAir - 0.1204*ΔHum + 0.0092*ΔRain + 0.0491*ΔSun - 0.9947*ΔWind - 4.1262*Δalbedo - 0.0003*DEM	0.53

Declaration of interests

☒ The authors declare that they have no known competing financial interests or personal relationships that could have appeared to influence the work reported in this paper.

☐The authors declare the following financial interests/personal relationships which may be considered as potential competing interests: